Journal of Computational Physics **156,** 43–88 (1999)
Article ID jcph.1999.6349, available online at http://www.idealibrary.com on IDEAL®

# A Fluid-Mixture Type Algorithm for Compressible Multicomponent Flow with van der Waals Equation of State

Keh-Ming Shyue

*Department of Mathematics, National Taiwan University, Taipei, Taiwan 106, Republic of China*
E-mail: shyue@math.ntu.edu.tw

Received September 17, 1998; revised May 19, 1999

In previous work by the author, a simple interface-capturing approach has been developed and validated for compressible multicomponent flows with a stiffened gas equation of state in multiple space dimensions. The algorithm uses a mixture type of the model equations written in a quasi-conservative form to ensure a consistent approximation of the energy equation near the interfaces where two or more fluid components are present in a grid cell. A standard high-resolution wave propagation method is employed to solve the proposed system, giving an efficient implementation of the algorithm. In this paper, the method is extended to a more general two-phase (liquid–gas) flow where the fluid of interests is characterized by a van der Waals-type equation of state. Several numerical results are presented in both one and two space dimensions that show the feasibility of the method with the Roe solver as applied to practical problems without introducing any spurious oscillations in the pressure near the interfaces. This includes a convergence study of a shock wave in liquid over a gas bubble. To deal with a difficult slip line problem where there is a strong shear flow moving along the interface, we implement the method based on the shock-only Riemann solver with an additional update by the scheme to the total kinetic energy. Rather than using solutions from the basic conservation laws for the density and momenta which incurs large errors, the resulting total kinetic energy is used to the computation of the pressure from the equation of state, yielding typically more accurate results than the unmodified method near the slip lines. This is demonstrated by numerical results of some sample two-dimensional Riemann problems. © 1999 Academic Press

*Key Words:* fluid-mixture algorithm; interface capturing method; multicomponent flow; slip line problems; stiffened gas equation of state; van der Waals gases.



0021-9991/99 $30.00
Copyright © 1999 by Academic Press
All rights of reproduction in any form reserved.

## 1. INTRODUCTION

This paper is concerned with the development of a simple interface-capturing approach for efficient numerical resolution of compressible multicomponent flows with a van der Waals-type fluid (i.e., a fluid with the finite size of a molecule and the nonzero cohesive forces between molecules [21]). We consider a simplified two-phase flow where the fluids of interest consist of two different phases, liquid and gas, separated by immiscible interfaces; see Fig. 1 for a sample setup in two space dimensions. The algorithm uses a Eulerian formulation of the equations in which, on the gas-phase part of the domain, the fluid is governed by the full set of the compressible Euler equations. In two space dimensions, for instance, it takes the form

$$\partial_t \begin{bmatrix} \rho \\ \rho u \\ \rho v \\ \rho E \end{bmatrix} + \partial_x \begin{bmatrix} \rho u \\ \rho u^2 + p \\ \rho uv \\ \rho Eu + pu \end{bmatrix} + \partial_y \begin{bmatrix} \rho v \\ \rho uv \\ \rho v^2 + p \\ \rho Ev + pv \end{bmatrix} = 0, \tag{1}$$

where $\rho$ is the density, $u$ and $v$ are the particle velocities in the $x$- and $y$-direction, respectively, $p$ is the pressure, and $E$ is the specific total energy. We assume that the gas satisfies a van der Waals equation of state,

$$p(\rho, e) = \left(\frac{\gamma - 1}{1 - b\rho}\right)(\rho e + a\rho^2) - a\rho^2, \tag{2}$$

so as to deal with the possible real-gas effect (without phase transitions) when both the temperature and pressure are high (cf. [21, 74, 78]). Here $e$ denotes the specific internal energy, $\gamma$ is the ratio of specific heats ($\gamma > 1$), and the quantities $a, b$ are the van der Waals gas constants for molecular cohesive forces and the finite size of molecules, respectively ($a \geq 0$, $0 \leq b < 1/\rho$, see [44] for numerical values to various gaseous substances). As usual we set $E = e + (u^2+v^2)/2$. Note that a van der Waals gas of the form (2) reduces to a Noble–Abel gas (also called a constant covolume gas) when $a = 0$ [54, 73] and to a polytropic gas when $b = 0$ as well. The four components of (1) express the conservation of mass, momenta in the $x$- and $y$-direction, and energy, respectively [15].

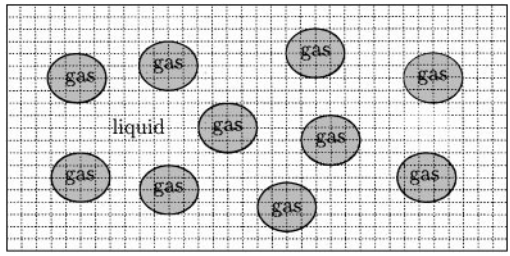


**FIG. 1.** A typical example of a two-phase flow setup with interfaces that separate regions of two different fluids, liquid and gas, into two parts. Note that the gas component in each elliptical-like shape of the domain may be different from one another. It is those grid cells that are cut by the interfaces requiring special attention for proper numerical treatments.

On the liquid-phase part of the domain, however, while the motion of a liquid is assumed to be governed by (1), the algorithm uses the stiffened gas equation of state,

$$p(\rho, e) = (\gamma - 1)\rho e - \gamma \mathcal{B}, \tag{3}$$

for a fundamental characterization of material properties of the liquids. Here $\mathcal{B}$ is a pressure-like constant that, together with $\gamma$, can be determined by a fitting procedure from laboratory data (cf. [47]). A typical set of parameter values is for water: $\gamma = 7$, $\mathcal{B} = 3000$ atm [15, 25], and for human blood: $\gamma = 5.527$, $\mathcal{B} = 614.6$ MPa [52], approximately. It should be mentioned that in addition to the modeling of a liquid, Eq. (3) is often used to describe other type of materials, including many compressible solids of practical importance (cf. [47, 55, 60]).

We want to use a state-of-the-art shock-capturing method on a uniform rectangular grid for the multicomponent flow computations. Clearly when grid cells contain only a single phase of the fluid, there is no problem to solve each phase of the equations separately. But in practice due to the presence and the subsequent dynamic-evolution of the interfaces by the solutions of the governing system, it is inevitable to have two or more fluid components staying within a cell (see Fig. 1). Because of this, the need to give a proper modeling and approximation of these mixture grid cells becomes a principle issue in many of the multicomponent algorithms developed in the literature (cf. [1, 12, 20, 29, 30, 46, 60, 63]). See [60] in particular for a concise survey of the up-to-date multicomponent methods.

The approach we take here is an extension of the work described by Saurel and Abgrall [60] and by the author [63, 64], in that as opposed to a simplier case with the stiffened gas equation of state (3), a modified van der Waals equation of state (5), see Section 2, is introduced as a basic element to the modeling of the mixing between the stiffened and van der Waals gases. With that, assuming uniform pressure equilibrium and constant particle velocity across the interfaces, from the energy equation, we are able to derive the effective equations for the mixture of the material-dependent quantities near the interfaces. As in the previous work [63], we take these equations to be of the form that do not vary their solutions across the shocks and rarefaction waves as well. Combining the resulting set of effective equations to the Euler equations yields a model system that is written in a quasi-conservative form; see (13) and (36) for the one- and two-dimensional models, respectively. We use the high-resolution wave propagation method developed by LeVeque [34, 39, 43] to solve the proposed system. Numerical results present in Sections 3.4 and 4.3 show that this is a viable approach in both one and two dimensions as the method is applied with the Roe solver to practical problems without introducing any spurious oscillations in the pressure near the interfaces.

To deal with a difficult slip line problem where there is a strong shear flow moving along the interface, we implement the two-dimensional method based on a shock-only Riemann solver with an additional update by the scheme to the total kinetic energy. Rather than using the solutions from the basic conservation laws for the density and momenta, which incurs large errors, see Section 5.1, the resulting total kinetic energy is employed to compute the pressure from the equation of state, yielding typically more accurate results than the unmodified method near slip lines. This will be discussed further in Section 5.2.

It is true that in many multicomponent flow applications physical effects, such as surface tension and viscosity, play an important role to not only controlling the dynamics of the interfaces, but also influencing the structure of the nearby solutions, and hence need to be

taken in the model for realization (cf. [66]). Typical examples of this kind are the popular water-drop problem in air and the rising air bubble problem in water. In these instances, because the fluids are mostly in a low Mach number regime, compressibility of the fluids is often ignored, and so the problem may be formulated into an incompressible form and solved by a state-of-the-art numerical method for incompressible flows; see [7, 68, 69, 75] for an example.

Here in contrast to the work just mentioned, we consider a class of problems where the influence of compressibility of the fluids to the solutions is vital, but not the surface tension and viscosity. Examples cover a family of shock wave problems with complicated interface patterns [24, 25, 53, 71, 76, 77] and a hydrodynamic model of sonoluminescence (an acoustic-induced light emission phenomenon) [8, 33, 78]. It is interesting to note that the latter problem in fact motivates the current study of two-phase flows with a van der Waals-type fluid where (2) is used for the modeling of real gases and (3) is employed for a simple approximation of liquids. Our goal here is to establish a basic solution strategy and validate its use via numerical experimentation of some sample problems. Direct simulation of sonoluminescence and other important two-phase flow problems such as shock waves in bubbly liquids or liquid–solid suspensions will be considered in the future; see [65] for a preliminary result of the latter problem.

This paper is organized as follows. In Section 2, we begin by discussing the basic equation of state and the associated thermodynamic stability for the mixing of the stiffened and van der Waals gases within a grid cell. In Section 3, we describe the one-dimensional version of the multicomponent algorithm in more details. This includes the construction of the Riemann problem solution by the shock-only or Roe solver (see Section 3.2) and some numerical results that validate the proposed approach (see Section 3.4). Extension of the basic approach to two space dimensions is explained briefly in Section 4, and some sample two-dimensional results are shown in Section 4.3. A study of how the algorithm works for slip line problems is addressed in Section 5.1, and a correction of the algorithm is made in Section 5.2.

## 2. EQUATIONS OF STATE

To begin, we introduce a hybrid version of the equation of state that is necessary in the algorithm for modeling the mixing between the stiffened and van der Waals gases within a grid cell. We do this by taking an approach that expresses (2) and (3) in terms of their natural variables: the specific entropy $S$ and the specific volume $V = 1/\rho$, yielding the formulas

$$p(V, S) = \mathcal{A}(S)(V - b)^{-\gamma} - aV^{-2}, \tag{4a}$$

and

$$p(V, S) = \mathcal{A}(S)V^{-\gamma} - \mathcal{B}, \tag{4b}$$

in a respective manner, where $\mathcal{A}(S) = \mathcal{R}\exp[(S - S_{\text{ref}})/C_V]$ takes the same form in both cases (cf. [21, 26]). Here $C_V$ represents the specific heat at constant volume (see below), $\mathcal{R}$ is the universal gas constant, and $S_{\text{ref}}$ is the reference state of the specific entropy. Assuming the fluids under consideration are all in an adiabatic equilibrium with the same entropy, it is feasible then to define an extension of the equation of state that combines (4a) with (4b)

in the following way:

$$p(V, S) = \mathcal{A}(S)(V - b)^{-\gamma} - (\mathcal{B} + aV^{-2}). \tag{4c}$$

With this, it is easy to see that not only the limiting van der Waals gas case (4a) is recovered as $\mathcal{B} \to 0$, but so also is the stiffened gas case (4b) as both $a \to 0$ and $b \to 0$. In the nonlimiting case, however, where none of the material-dependent quantities $a$, $b$, and $\mathcal{B}$ is close to zero, (4c) does give a way to the representation of the cases in between, that is to the mixing of the stiffened and van der Waals gases.

It should be noted that, as far as the computational efficiency of the method is concerned, (4c) is of little use in practice, for it requires some extra work to evaluate the specific entropy from the solutions of the Euler equations. Instead, by employing the first and second laws of thermodynamics, we may rewrite (4c) in terms of the often-used variables in gas dynamics, $\rho$ and $e$, as

$$p(\rho, e) = \left(\frac{\gamma - 1}{1 - b\rho}\right)(\rho e - \mathcal{B} + a\rho^2) - (\mathcal{B} + a\rho^2). \tag{5}$$

It is clear that (5) is a generalization of the equations of state (2) and (3). As we will see in the latter sections (cf. [64, 65] also for a simpler case), with this so-called modified van der Waals equation of state (5), it is very robust to devise an interface-capturing solver for a family of two-phase flow problems considered here.

As to the computation of the fluid temperature $T$ (which is important to sonoluminescence, for example), with (5), we may simply use one of the formulas,

$$p(V, T) = \frac{\mathcal{R}T}{V - b} - \mathcal{B} - \frac{a}{V^2},$$
$$e(V, T) = \frac{\mathcal{R}T}{\gamma - 1} + \mathcal{B}V - \frac{a}{V},$$

for realization. Note that these two equations are easily derived from (5) using the basic thermodynamic principles; see [21] for more details.

It is important to mention that, in this work, the thermodynamic description of the multicomponent flows is limited by the stability requirement that the internal energy defined in (5) be a convex function of its dependent variables $V$ and $S$. Because of this, the immediate consequence is the exclusion of the important but difficult problems involving the transition of phases here. Analogously in [49, 50] for a Mie–Grüneisen-type equation of state (see below), it can be shown that explicit conditions for the above mentioned thermodynamic stability of a van der Waals gas are

(i) The heat capacity coefficients $C_V$ and $C_p$ must be positive,

$$C_V = (\partial_T e)|_V = \frac{\mathcal{R}}{\gamma - 1} > 0,$$
$$C_p = (\partial_T h)|_p = \frac{\mathcal{R}[\gamma\mathcal{R}T - 2a\rho(1 - b\rho)^2]}{(\gamma - 1)[\mathcal{R}T - 2a\rho(1 - b\rho)^2]} > 0,$$

where $h = e + (p/\rho)$ is the specific enthalpy.

(ii) The isentropic bulk modulus $K_S$ must be positive,

$$K_S = \rho(\partial_\rho p)|_S = \left(\frac{\gamma}{1-b\rho}\right)(p + \mathcal{B} + a\rho^2) - 2a\rho^2 > 0.$$

(iii) The product of the thermal expansion coefficient $\vartheta$ and the Grüneisen coefficient $\Gamma$ must be nonnegative,

$$\begin{aligned}\vartheta\Gamma &= \left[-\frac{1}{\rho}(\partial_T \rho)\Big|_p\right]\left[\frac{1}{\rho}(\partial_e p)\Big|_\rho\right] \\ &= \left[\frac{\mathcal{R}(1-b\rho)}{\mathcal{R}T - 2a\rho(1-b\rho)^2}\right]\left[\frac{\gamma-1}{1-b\rho}\right] = \frac{\mathcal{R}(\gamma-1)}{\mathcal{R}T - 2a\rho(1-b\rho)^2} \geq 0.\end{aligned}$$

In summary, for stability, from the above conditions, this amounts to the satisfaction of the inequalities

$$\gamma > 1, \quad \mathcal{R}T > 2a\rho(1-b\rho)^2.$$

Combining this with the positiveness of the basic thermodynamic states, $\rho$, $T$, and $\Gamma$, defines the domain of the phase space of this van der Waals gas model. Note in particular that from item (ii) given above we have $K_S = \rho c^2$, and so the positive of $K_S$ implies that the speed of sound $c$ belongs to a set of real numbers.

For convenience, we write (5) into a more general Mie–Grüneisen-type equation of state of the form

$$p(\rho, e) = \Gamma(\rho)[\rho e - \rho e_H(\rho)] - p_H(\rho), \tag{6}$$

where $\Gamma$ is the Grüneisen coefficient of the material of interests, and the density-dependent functions $e_H$, $p_H$ are the reference Hugoniot states. Typically, the specific form of (6) is rather complicated in general (cf. [27, 28, 48]). Here for fluids described by (5), we have a relatively simple but nontrivial model to work with, i.e.,

$$\Gamma(\rho) = \frac{\gamma-1}{1-b\rho}, \quad e_H(\rho) = \frac{\mathcal{B} - a\rho^2}{\rho}, \quad p_H(\rho) = \mathcal{B} + a\rho^2. \tag{7}$$

It is without question that experience gained by studying the current van der Waals gas model will help to the further development of an efficient multicomponent solver for more general materials as described by (6).

## 3. ONE SPACE DIMENSION

To motivate the basic idea of our method in multiple space dimensions, we begin by considering one-dimensional problems with both the gas and the liquid governed by the Euler Eqs. (1) of the following form in the $x$-direction,

$$\partial_t \begin{bmatrix} \rho \\ \rho u \\ \rho E \end{bmatrix} + \partial_x \begin{bmatrix} \rho u \\ \rho u^2 + p \\ \rho E u + p u \end{bmatrix} = 0, \tag{8}$$

and by the equations of state (2) and (3), respectively. The algorithm uses a popular approach that employs (8) for the motion of the liquid–gas mixtures of the conserved variables $\rho$, $\rho u$, and $\rho E$ in a multicomponent grid cell (see [1, 61, 79] for the use of other governing equations). We compute the pressure based on the equation of state (6), so long as the mixture of the problem-dependent material quantities appearing in (7), i.e., $\gamma$, $a$, $b$, and $\mathcal{B}$, are defined and known a priori as well. In the algorithm, by following a general procedure proposed in [63], conditions for those material quantities are found so that not only the pressure is retained in equilibrium for an interface only fluid-mixture cell, but also the mixture of the total mass remains conservative on the domain (of course, the mass of each fluid component may not typically be conserved here). For completeness, we next give a detailed description of that procedure.

### 3.1. *Derivation of Model Equations*

As in the previous works [63, 64], our starting point is to consider an interface only problem where both the pressure $p$ and particle velocity $u$ are constants in the domain (i.e., $p$ and $u$ satisfy the standard surface-tension free dynamic and kinematic boundary conditions on the interface [32], respectively), while the other variables such as the density $\rho$ and the material-dependent parameters in the Mie–Grüneisen equation of state (6) are having jumps across some interfaces. In this setup, we first write (8) in the following nonconservative form,

$$\begin{aligned}\partial_t \rho + u\partial_x \rho + \rho \partial_x u &= 0,\\ \partial_t u + u\partial_x u + \frac{1}{\rho}\partial_x p &= 0,\\ \partial_t(\rho e) + \partial_x(\rho e u) + p\partial_x u &= 0,\end{aligned}$$

and obtain easily two basic transport equations for the motion of $\rho$ and $\rho e$ as

$$\begin{aligned}\partial_t \rho + u\partial_x \rho &= 0,\\ \partial_t(\rho e) + u\partial_x(\rho e) &= 0.\end{aligned}$$

By inserting the equation of state (6) into the latter one, we find an alternative description of the energy equation

$$\partial_t\left(\frac{p+p_H}{\Gamma}+\rho e_H\right)+u\partial_x\left(\frac{p+p_H}{\Gamma}+\rho e_H\right)=0. \tag{9}$$

To see how the pressure would retain in equilibrium as it should be for this model problem, we expand (9) into the form

$$\frac{1}{\Gamma}(\partial_t p+u\partial_x p)+p\left[\partial_t\left(\frac{1}{\Gamma}\right)+u\partial_x\left(\frac{1}{\Gamma}\right)\right]+\left[\partial_t\left(\frac{p_H}{\Gamma}+\rho e_H\right)+u\partial_x\left(\frac{p_H}{\Gamma}+\rho e_H\right)\right]=0.$$

Applying the assumed state of the pressure equilibrium to the above equation comes to a simplier expression as

$$p\left[\partial_t\left(\frac{1}{\Gamma}\right)+u\partial_x\left(\frac{1}{\Gamma}\right)\right]+\left[\partial_t\left(\frac{p_H}{\Gamma}+\rho e_H\right)+u\partial_x\left(\frac{p_H}{\Gamma}+\rho e_H\right)\right]=0.$$

Now since this equation should hold for any $p$ in the physical space, it implies right away that the terms in the square bracket of the equation should be vanished simultaneously, yielding a system of the following two equations:

$$\partial_t\left(\frac{1}{\Gamma}\right) + u\partial_x\left(\frac{1}{\Gamma}\right) = 0, \tag{10a}$$

$$\partial_t\left(\frac{p_H}{\Gamma} + \rho e_H\right) + u\partial_x\left(\frac{p_H}{\Gamma} + \rho e_H\right) = 0. \tag{10b}$$

It is important to note that in order to have the correct pressure equilibrium in (9) near the interfaces, (10a) and (10b) are the two key equations that should be satisfied for any given expression of $\Gamma$, $p_H$, and $e_H$ in the Mie–Grüneisen equation of state (6). From them, for a class of real materials modeled analytically by (6) at least, we may continue to work out suitable conditions for the further details of the related material parameters.

Consider the current two-phase flow application with $\Gamma$, $p_H$, and $e_H$ defined by (7), for example. Equations (10a) and (10b) now have the form

$$\partial_t\left(\frac{1-b\rho}{\gamma-1}\right) + u\partial_x\left(\frac{1-b\rho}{\gamma-1}\right) = 0, \tag{11a}$$

$$\partial_t\left(\frac{\gamma-b\rho}{\gamma-1}\mathcal{B} + \frac{2-\gamma-b\rho}{\gamma-1}a\rho^2\right) + u\partial_x\left(\frac{\gamma-b\rho}{\gamma-1}\mathcal{B} + \frac{2-\gamma-b\rho}{\gamma-1}a\rho^2\right) = 0, \tag{11b}$$

in a respective manner. It is obvious that, in addition to (11a) and (11b), we need to impose two supplementary conditions so as to have enough equations for the four material quantities: $\gamma$, $a$, $b$, and $\mathcal{B}$. In our approach, this is done quite easily by simply splitting (11a) into the following two parts,

$$\partial_t\left(\frac{1}{\gamma-1}\right) + u\partial_x\left(\frac{1}{\gamma-1}\right) = 0, \tag{11c}$$

$$\partial_t\left(\frac{b\rho}{\gamma-1}\right) + u\partial_x\left(\frac{b\rho}{\gamma-1}\right) = 0, \tag{11d}$$

and also (11b) into the terms

$$\partial_t\left(\frac{\gamma-b\rho}{\gamma-1}\mathcal{B}\right) + u\partial_x\left(\frac{\gamma-b\rho}{\gamma-1}\mathcal{B}\right) = 0, \tag{11e}$$

$$\partial_t\left(\frac{2-\gamma-b\rho}{\gamma-1}a\rho^2\right) + u\partial_x\left(\frac{2-\gamma-b\rho}{\gamma-1}a\rho^2\right) = 0. \tag{11f}$$

Having done so, we arrive at a primitive form of the transport equations (11c)–(11f) for the variables $1/(\gamma-1)$, $b\rho/(\gamma-1)$, $\mathcal{B}(\gamma-b\rho)/(\gamma-1)$, and $a\rho^2(2-\gamma-b\rho)/(\gamma-1)$. We note that with them for this interface only problem it is sufficient to have all the quantities $\gamma$, $a$, $b$, and $\mathcal{B}$ determined at all times, provided that the initial condition has been properly set for the computation; see Section 3.1.1.

Up to this point, our discussion stresses only on an approach that is capable of maintaining the pressure in equilibrium for a model interface only problem. Since in practice we are

interested in shock wave problems as well, we should thus take the equations, i.e., (11c)–(11f), in a form such that $\gamma$, $a$, $b$, and $\mathcal{B}$ remain unchanged across both shocks and rarefaction waves. Concerning this, it is easy to see that with $\gamma$ governed by (11c) there is no problem to do so (cf. [1, 63]). For $b$ and $\mathcal{B}$, however, due to the appearance of the linear factor of $\rho$ in (11d) and (11e), it turns out that, in a time when such a scenario occurs, for consistency these two equations should be modified in such a way that each of them reduces to the basic mass conservation law of the fluid mixture. The derivation of the modification is simple. Without going into the details, we write down the corrected version of the corresponding equation as follows:

$$\partial_t\left(\frac{b\rho}{\gamma-1}\right)+\partial_x\left(\frac{b\rho}{\gamma-1}u\right)=0, \tag{12a}$$

$$\partial_t\left(\frac{\gamma-b\rho}{\gamma-1}\mathcal{B}\right)+\partial_x\left(\frac{\gamma-b\rho}{\gamma-1}\mathcal{B}u\right)=\left(\frac{\gamma}{\gamma-1}\mathcal{B}\right)\partial_x u. \tag{12b}$$

We next come to the discussion for the quantity $a$ described by (11f). In this situation, if we assume the proper smoothness of the nonlinear factors of $\rho$ in the equation (such as in the case of rarefaction waves), as in (12a) and (12b) for the quantities $b$ and $\mathcal{B}$, respectively, we may derive an equation of the form

$$\partial_t\left(\frac{2-\gamma-b\rho}{\gamma-1}a\rho^2\right)+\partial_x\left(\frac{2-\gamma-b\rho}{\gamma-1}a\rho^2u\right)=-\left(\frac{2-\gamma-2b\rho}{\gamma-1}a\rho^2\right)\partial_x u \tag{12c}$$

that admits the desired constancy of $a$ and the mass conservation as well. It is important to note that this is not the case, however, if the smoothness assumption on $\rho$ is violated; this happens in the event of shock waves, for there is no way to differentiate the discontinuous terms $\rho^2$ and $\rho^3$ yielding the partial derivatives on $\rho$ itself. Despite its apparent difficulty to fulfill the requirement of $a$ across both shocks and rarefaction waves, (12c) is the correct form to be used in the model so that the fluid mixture $a\rho^2(2-\gamma-b\rho)/(\gamma-1)$ can be solved and applied readily to the computation of the pressure; see (14) below.

Here, rather than using (12c), we introduce a simplier linear advection equation of the form

$$\partial_t a+u\partial_x a=0 \tag{12d}$$

for the motion of the mixture of $a$. Clearly, (12d) gives an accurate description of $a$ in all the solution regions discussed above. In practice, it is a good one to use in the algorithm for numerical approximation, see Section 3.4 for some sample results.

To sum up, as in [63], we use the term effective equations to describe the set of equations that govern the motion of the material-dependent mixtures of the problems. In the current case, there consists of a couple sytem of five equations, i.e., (11c) and (12a)–(12d). It should be noted that when further taking the numerical aspect of the model approximation into consideration, with the full Euler equations, these effective equations are the proper ones to use for practical problems, but not the other form of the equations; see Section 3.3 and [60, 63] for the details.

Putting all the things together, with the modified van der Waals equation of state (5), the model equations we propose to solve one-dimensional multicomponent problems are

$$\begin{cases} \partial_t \rho + \partial_x(\rho u) = 0 \\ \partial_t(\rho u) + \partial_x(\rho u^2 + p) = 0 \\ \partial_t(\rho E) + \partial_x(\rho E u + p u) = 0 \\ \partial_t\left(\frac{b\rho}{\gamma-1}\right) + \partial_x\left(\frac{b\rho}{\gamma-1}u\right) = 0 \\ \partial_t\left(\frac{\gamma-b\rho}{\gamma-1}\mathcal{B}\right) + \partial_x\left(\frac{\gamma-b\rho}{\gamma-1}\mathcal{B}u\right) = \left(\frac{\gamma\mathcal{B}}{\gamma-1}\right)\partial_x u \\ \partial_t\left(\frac{2-\gamma-b\rho}{\gamma-1}a\rho^2\right) + \partial_x\left(\frac{2-\gamma-b\rho}{\gamma-1}a\rho^2 u\right) = -\left(\frac{2-\gamma-2b\rho}{\gamma-1}a\rho^2\right)\partial_x u \\ \partial_t\left(\frac{1}{\gamma-1}\right) + u\partial_x\left(\frac{1}{\gamma-1}\right) = 0 \\ \partial_t a + u\partial_x a = 0; \end{cases} \tag{13}$$

this gives us eight equations in total to be solved in one space dimension that is nicely independent of the number of fluid components involved in the problem. It is clear that in this system the first three are the Euler equations which are used to make certain the conservation of the basic fluid mixtures, $\rho$, $\rho u$, and $\rho E$, while the remaining are the effective equations that are introduced to ensure the correct mixing of the problem-dependent material variables near the interfaces. With a system expressed in this way, there is no problem to compute all the state variables of interest, including the pressure from the equation of state

$$p = \left[\rho E - \frac{(\rho u)^2}{2\rho} - \left(\frac{\gamma-b\rho}{\gamma-1}\mathcal{B}\right) - \left(\frac{2-\gamma-b\rho}{\gamma-1}a\rho^2\right)\right] \Big/ \left(\frac{1}{\gamma-1} - \frac{b\rho}{\gamma-1}\right). \tag{14}$$

Note that (13) reduces to a well-tested $\gamma$-based model for a stiffened gas when $a = b = 0$ (cf. [60, 63, 64]) and for a polytropic gas when $\mathcal{B} = 0$ as well (cf. [1]). As before, the proposed system (13) is not written in the full conservation form, but is rather a quasi-conservative system of equations. In addition, the nonzero terms on the right-hand side of the fifth and sixth equations of (13) should be viewed as an integrated part of the whole system, but not be considered as a source term. This fact can be realized easily by formulating the model as a quasi-linear system of equations (of course, with the assumption of a proper smoothness of the solutions), namely,

$$\partial_t q + A(q)\partial_x q = 0 \tag{15a}$$

with the state vector

$$q = \left[\rho, \rho u, \rho E, \frac{b\rho}{\gamma-1}, \frac{\gamma-b\rho}{\gamma-1}\mathcal{B}, \frac{2-\gamma-b\rho}{\gamma-1}a\rho^2, \frac{1}{\gamma-1}, a\right]^T \tag{15b}$$

and the matrix

$$A(q) = \begin{bmatrix} 0 & 1 & 0 & 0 & 0 & 0 & 0 & 0 \\ K-u^2 & u(2-\Gamma) & \Gamma & p\Gamma & -\Gamma & -\Gamma & -p\Gamma & 0 \\ u(K-H) & H-u^2\Gamma & u(\Gamma+1) & up\Gamma & -u\Gamma & -u\Gamma & -up\Gamma & 0 \\ -\varphi u & \varphi & 0 & u & 0 & 0 & 0 & 0 \\ \varphi u\mathcal{B} & -\varphi\mathcal{B} & 0 & 0 & u & 0 & 0 & 0 \\ -\chi u & \chi & 0 & 0 & 0 & u & 0 & 0 \\ 0 & 0 & 0 & 0 & 0 & 0 & u & 0 \\ 0 & 0 & 0 & 0 & 0 & 0 & 0 & u \end{bmatrix}. \quad (15c)$$

Here $K = \Gamma u^2/2$, $H = E + (p/\rho)$, $\varphi = b/(\gamma - 1)$, and $\chi = a\rho(4 - 2\gamma - 3b\rho)/(\gamma - 1)$. Recall that $\Gamma$ is the Grüneisen coefficient, see (7), which gives different values for different fluids.

It is easy to show that for each physically relevant value of the state variables $q$ defined in the region of thermodynamic stability (see Section 2), the eigenstructure of the matrix $A$ is possessed of real eigenvalues

$$\Lambda = \operatorname{diag}(\lambda_1, \lambda_2, \ldots, \lambda_8) = \operatorname{diag}(u - c, u, u + c, u, \ldots, u) \quad (16a)$$

and a complete set of eigenvectors of the form

$$R = (r_1, r_2, \ldots, r_8) = \begin{bmatrix} 1 & 1 & 1 & 0 & 0 & 0 & 0 & 0 \\ u-c & u & u+c & 0 & 0 & 0 & 0 & 0 \\ H-uc & \frac{1}{2}u^2 & H+uc & -p & 1 & 1 & p & 0 \\ \varphi & 0 & \varphi & 1 & 0 & 0 & 0 & 0 \\ \varphi\mathcal{B} & 0 & \varphi\mathcal{B} & 0 & 1 & 0 & 0 & 0 \\ \chi & 0 & \chi & 0 & 0 & 1 & 0 & 0 \\ 0 & 0 & 0 & 0 & 0 & 0 & 1 & 0 \\ 0 & 0 & 0 & 0 & 0 & 0 & 0 & 1 \end{bmatrix} \quad (16b)$$

with $Ar_k = \lambda_k r_k$. Thus, (15a) is a hyperbolic system of partial differential equations and so is our multicomponent model (13). Regarding discontinuous solutions of the system, such as shock waves or contact discontinuities, (13) has the usual form of the Rankine–Hugoniot jump conditions across the waves; see Section 3.2.1 for more details.

With these comments, it should be sensible to use the proposed model for practical computations. The numerical method to be discussed in Section 3.3 is a consistent approximation of the model that gives excellent results for a wide variety of problems as illustrated in Section 3.4.

*3.1.1. Initialization of fluid-mixture cells.* Consider a typical multicomponent setting in which there are $m$ different fluids in a grid cell, and each of them occupies a distinct region with a volume-fraction function $Y^{(i)}$ in relation to it, for $i = 1, 2, \ldots, m$. Here by the standard assumption, we have $Y^{(i)} \in [0, 1]$ and $\sum_{i=1}^{m} Y^{(i)} = 1$. Suppose that for each component $i$ the state variables such as $\rho^{(i)}$, $u^{(i)}$, $p^{(i)}$, $\gamma^{(i)}$, $a^{(i)}$, $b^{(i)}$, and $\mathcal{B}^{(i)}$ are known a priori. The objective is to give a proper definition of the fluid mixtures so that they can be used as an initial condition for our model equations (13) to the computations.

In the algorithm, we follow a common practice by evaluating the mixing states $\rho$, $\rho u$, and $\rho e$ as a volume-weighted sum over the set of components $\rho^{(i)}$, $\rho^{(i)}u^{(i)}$, and $\rho^{(i)}e^{(i)}$ given above,

$$\begin{bmatrix} \rho \\ \rho u \\ \rho e \end{bmatrix} = \sum_{i=1}^{m} Y^{(i)} \begin{bmatrix} \rho^{(i)} \\ \rho^{(i)}u^{(i)} \\ \rho^{(i)}e^{(i)} \end{bmatrix}. \tag{17}$$

With this result, we then compute the mixture of the total energy by $\rho E = \rho e + (\rho u)^2/(2\rho)$; this completes the definition of the conservative variables for the first three equations of the model.

To find the initial fluid mixtures, $1/(\gamma - 1)$, $b\rho/(\gamma - 1)$, $\mathcal{B}(\gamma - b\rho)/(\gamma - 1)$, and $a\rho^2(2 - \gamma - b\rho)/(\gamma - 1)$, for the next four equations, we use the equation of state (5), where written as a function of the volume fraction it reads

$$\left(\frac{1 - b\rho}{\gamma - 1}\right)(p + \mathcal{B} + a\rho^2) + \mathcal{B} - a\rho^2 = \rho e = \sum_{i=1}^{m} Y^{(i)}\rho^{(i)}e^{(i)}$$
$$= \sum_{i=1}^{m} Y^{(i)}\left[\left(\frac{1 - b^{(i)}\rho^{(i)}}{\gamma^{(i)} - 1}\right)(p^{(i)} + \mathcal{B}^{(i)} + a^{(i)}(\rho^{(i)})^2) + \mathcal{B}^{(i)} - a^{(i)}(\rho^{(i)})^2\right].$$

By taking a similar approach as employed in Section 3.1 for the derivation of the effective equations, it comes out easily a splitting of the above equation into the form

$$\begin{bmatrix} \frac{1}{\gamma - 1} \\ \frac{b\rho}{\gamma - 1} \\ \frac{\gamma - b\rho}{\gamma - 1}\mathcal{B} \\ \frac{2 - \gamma - b\rho}{\gamma - 1}a\rho^2 \end{bmatrix} = \sum_{i=1}^{m} Y^{(i)} \begin{bmatrix} \frac{1}{\gamma^{(i)} - 1} \\ \frac{b^{(i)}\rho^{(i)}}{\gamma^{(i)} - 1} \\ \frac{\gamma^{(i)} - b^{(i)}\rho^{(i)}}{\gamma^{(i)} - 1}\mathcal{B}^{(i)} \\ \frac{2 - \gamma^{(i)} - b^{(i)}\rho^{(i)}}{\gamma^{(i)} - 1}a^{(i)}(\rho^{(i)})^2 \end{bmatrix}, \tag{18}$$

where in the process of splitting the terms the pressure $p$ is chosen to satisfy the relation as

$$\left(\frac{1 - b\rho}{\gamma - 1}\right)p = \sum_{i=1}^{m} Y^{(i)}\left[\left(\frac{1 - b^{(i)}\rho^{(i)}}{\gamma^{(i)} - 1}\right)p^{(i)}\right] \tag{19}$$

(cf. [63] also for a simplier case of how this is done). With (18), it is easy to see that when each of the partial pressures is in equilibrium within a grid cell, the pressure p acquired from (19) would remain in equilibrium also; i.e., $p = p^{(i)}$, for $i = 1, 2, \ldots, m$. Furthermore, from (18), we are able to obtain an explicit expression of the material-dependent parameters $\gamma$, $a$, $b$, and $\mathcal{B}$ in terms of the volume-fraction function and the original set of data. The results are

$$\gamma = 1 + 1 \Bigg/ \left(\sum_{i=1}^{m} \frac{Y^{(i)}}{\gamma^{(i)} - 1}\right), \tag{20a}$$

$$b = \left[\sum_{i=1}^{m} Y^{(i)}\left(\frac{b^{(i)}\rho^{(i)}}{\gamma^{(i)} - 1}\right)\right] \Bigg/ \left[\left(\sum_{i=1}^{m} Y^{(i)}\rho^{(i)}\right)\left(\sum_{i=1}^{m} \frac{Y^{(i)}}{\gamma^{(i)} - 1}\right)\right], \tag{20b}$$

$$\mathcal{B} = \left[\sum_{i=1}^{m} Y^{(i)}\left(\frac{\gamma^{(i)} - b^{(i)}\rho^{(i)}}{\gamma^{(i)} - 1}\mathcal{B}^{(i)}\right)\right] \Bigg/ \left[1 + \sum_{i=1}^{m} Y^{(i)}\left(\frac{1 - b^{(i)}\rho^{(i)}}{\gamma^{(i)} - 1}\right)\right], \tag{20c}$$

$$a = \left[\sum_{i=1}^{m} Y^{(i)}\left(\frac{2 - \gamma^{(i)} - b^{(i)}\rho^{(i)}}{\gamma^{(i)} - 1}a^{(i)}(b^{(i)})^2\right)\right] \Bigg/ \left\{\left(\sum_{i=1}^{m} Y^{(i)}\rho^{(i)}\right)^2 \times \left[-1 + \sum_{i=1}^{m} Y^{(i)}\left(\frac{1 - b^{(i)}\rho^{(i)}}{\gamma^{(i)} - 1}\right)\right]\right\}. \tag{20d}$$

We note that as in the continuous counterpart (12c), (20d) is not used in practice for setting the initial mixture of $a$, but is done by the formula $a = \sum_{i=1}^{m} Y^{(i)}a^{(i)}$ instead.

To end this subsection, it should be mentioned that by following the same approach introduced in [63] we may reformulate the model (13) into its variant form, the so-called volume-fraction model, that is robust when both the set of governing equations and the type of equations of state are different from one fluid component to the others, separated by the interfaces. To keep the presentation simple and clear, we omit the discussion of that model here, but refer the reader to [64, 65] for the details.

### 3.2. *Approximate Riemann Solvers*

Before describing numerical methods to solve (13), we pause to discuss the construction of the Riemann problem solutions which is one of the major steps in our multicomponent algorithm. For comparison purposes, we present two popular approaches for the resolution of the Riemann problem with piecewise constant data $q_L$ and $q_R$ to the left and right of the interface.

*3.2.1. Shock-only solver.* First, we are concerned with a shock-only approximation of the Riemann solver that ignores the possibility of rarefaction waves and simply construct a solution in which each pair of the states is connected along the Hugoniot locus for a shock (cf. [3, 10, 13]). In this approach, the key step is to find the midstate $(u_*, p_*)$ in the $u$–$p$ phase plane so that it can connect to $(u_L, p_L)$ by a 1-shock and to $(u_R, p_R)$ by a 3-shock. It is well known that this is equivalent to solving the following nonlinear equation in an iterative manner for the pressure $p_*$:

$$h(p_*) = u_{*R}(p_*) - u_{*L}(p_*) = 0. \tag{21}$$

Here $u_{*L}$ and $u_{*R}$ are the velocities defined by connecting the states along the 1-shock and 3-shock curves, respectively,

$$u_{*L}(p) = u_L - \frac{p - p_L}{M_L(p)}, \quad u_{*R}(p) = u_R + \frac{p - p_R}{M_R(p)},$$

with $M_\iota$ denoting the Lagrangian shock speed, for $\iota = L$ or $R$. In the current application with the modified van der Waals equation of state (5), when $a = 0$ (i.e., the vanishing of the $a\rho^2$ term), we may compute $M_\iota$ directly by evaluating the formula

$$M_\iota^2(p) = C_\iota^2\left[1 + \left(\frac{\gamma_\iota + 1}{2\gamma_\iota}\right)\left(\frac{p + \mathcal{B}_\iota}{p_\iota + \mathcal{B}_\iota} - 1\right)\right],$$

where $C_\iota = \rho_\iota c_\iota$ is the Lagrangian sound speed (cf. [73]). Note that this is as a result derived from the Rankine–Hugoniot jump condition across the shock waves,

$$M_\iota^2(e_{*\iota} - e_\iota) = \left(p_*^2 - p_\iota^2\right)/2, \tag{22}$$

with $e_{*\iota} = e(p_*, \rho_{*\iota})$ a function of the midstate density $\rho_{*\iota}$, a quantity that is related to $p$, $p_\iota$, and $M_\iota$ in the following way

$$\rho_{*\iota}(p) = \left[\rho_\iota^{-1} - \frac{p - p_\iota}{M_\iota^2(p)}\right]^{-1},$$

while in the more general case when $a \neq 0$, there is not such a close form solution available for $W_\iota$. Instead, we need to solve (22) iteratively for $M_\iota$; this is a typical thing to do when using the method for real gases (cf. [13]).

When applying a standard root-finding approach such as the secant method to (21), we have a 2-step iteration scheme as follows,

$$p_*^{(n+1)} = p_*^{(n)} - \frac{\left|p_*^{(n)} - p_*^{(n-1)}\right|}{\left|u_{*L}^{(n)} - u_{*L}^{(n-1)}\right| + \left|u_{*R}^{(n)} - u_{*R}^{(n-1)}\right|}\left[u_{*R}^{(n)} - u_{*L}^{(n)}\right], \tag{23}$$

where $u_{*\iota}^{(n)} = u_{*\iota}[p_*^{(n)}]$, for $\iota = L$ or $R$, and $n = 1, 2, \ldots$ (until convergence). With a suitable choice of the starting values $p_*^{(0)}$ and $p_*^{(1)}$, method (23) typically converges to the exact solution $p_*$ at a superlinear rate [31]. For gas dynamics, it is a common practice to set $p_*^{(0)}$ and $p_*^{(1)}$ by

$$\begin{aligned} p_*^{(0)} &= \frac{p_R C_L + p_L C_R - (u_R - u_L) C_L C_R}{C_L + C_R}, \\ u_{*L}^{(0)} &= u_L - \frac{p_*^{(0)} - p_L}{C_L}, \quad u_{*R}^{(0)} = u_R + \frac{p_*^{(0)} - p_R}{C_R}, \\ p_*^{(1)} &= \frac{p_R M_L^{(0)} + p_L M_R^{(0)} - (u_R - u_L) M_L^{(0)} M_R^{(0)}}{M_L^{(0)} + M_R^{(0)}}, \end{aligned} \tag{24}$$

with $M_\iota^{(0)} = M_\iota[p_*^{(0)}]$. After a satisfactory convergence of the scheme, we may then calculate $u_*$ by

$$u_* = \frac{p_L - p_R + u_L M_L(p_*) + u_R M_R(p_*)}{M_L(p_*) + M_R(p_*)}.$$

We note that alternatively we may use a 1-step Newton method for the solution of (21). Since the derivation of the scheme is more involved due to the need to compute the derivative term $dp_*/du_*$, we do not discuss the method here, but refer the reader to [13] for more details.

Figure 2 shows a typical solution structure of the Riemann problem considered here. Clearly, in a shock-only approximate solver, we replace the leftward-going rarefaction wave by a 1-shock and so the solution consists of three discontinuities moving at constant speeds. Here the propagation speed of each discontinuity is determined by

$$\lambda_1 = u_* - \frac{M_L(p_*)}{\rho_{*L}(p_*)}, \quad \lambda_2 = u_*, \quad \lambda_3 = u_* + \frac{M_R(p_*)}{\rho_{*R}(p_*)}, \tag{25a}$$

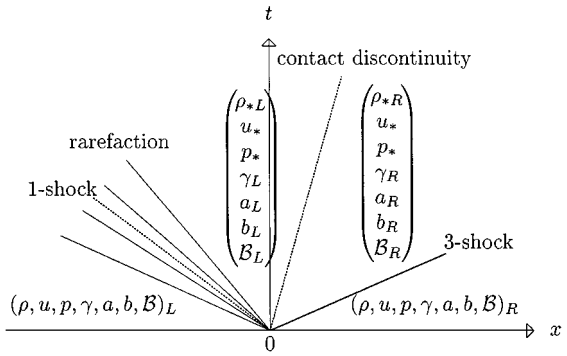


**FIG. 2.** Typical solution structure of the Riemann problem for our multicomponent model (13). Note that in a shock-only approximation of the approximate Riemann solver, the rarefaction wave is replaced by an entropy-violating shock.

with the jumps across each of them computed by the difference between the states to the left and right of the discontinuity,

$$\mathcal{W}_1 = q_{*L} - q_L, \quad \mathcal{W}_2 = q_{*R} - q_{*L}, \quad \mathcal{W}_3 = q_R - q_{*R}. \tag{25b}$$

Wave propagation methods are based on using these propagating discontinuities to update the cell averages in the cells neighboring each interface.

It is true that no matter what iterative method is employed to the solution of (21), the approach is quite expansive as compared to the approximate solver of Roe described next. Nevertheless, there are various situations where this approach is worthwhile and can provide more accurate results than the Roe solver does. This includes some examples shown in [18, 41, 56] and many difficult problems with strong shock waves and stiff equations of state. Moreover, it is a straightforward matter to generalize the approach that covers the case with surface tension effect across the interfaces; results on this aspect will be reported elsewhere.

*3.2.2. Roe solver.* In a Roe's approximate Riemann solver, we replace the nonlinear system (13) with data $q_L$ and $q_R$ by a linear system of the form

$$\partial_t q + \hat{A}(q_L, q_R)\partial_x q = 0. \tag{26}$$

Here $\hat{A}(q_L, q_R)$ is a constant matrix that depends on the initial data and is a local linearization of the matrix $A$ in (15c) about an average state. To find that matrix, as it is often done in many other Roe solvers (cf. [9, 22, 23]), we want to seek an average state such that the difference of the fluxes in the conservation part of (13) (i.e., the first four equations of the system) are equal to the respective first order approximations of the flux differences. That is,

$$\Delta\mathcal{F}^{(i)} = (\mathcal{F}_R - \mathcal{F}_L)^{(i)} = [\hat{A}(q_L, q_R)(q_R - q_L)]^{(i)} = [\hat{A}(q_L, q_R)\Delta q]^{(i)}, \tag{27}$$

for $i = 1, 2, 3, 4$, where $\mathcal{F} \in \mathbb{R}^4$ is the usual definition of the fluxes for conservation laws, and $\Delta\mathcal{F}^{(i)}$ is the $i$th component of $\Delta\mathcal{F}$. With that, it is a straightforward matter to obtain the results for $\hat{u}$, $\hat{H}$, and $\hat{\varphi}$ by the standard "Roe-averaging" approach; i.e., for a given pair $(\rho_L, \rho_R)$, the average state for a quantity $z$ is defined by

$$\hat{z} = \frac{\sqrt{\rho_L}z_L + \sqrt{\rho_R}z_R}{\sqrt{\rho_L} + \sqrt{\rho_R}}. \tag{28}$$

Note that in the process of the derivation, as in [63] we have chosen the averages $\widehat{(1/\Gamma)}$ and $\widehat{(p/\Gamma)}$ based on (28) so that the expression

$$\Delta p = \left[\widehat{\left(\frac{1}{\Gamma}\right)}\,\Delta\left(\frac{p}{\Gamma}\right) - \widehat{\left(\frac{p}{\Gamma}\right)}\,\Delta\left(\frac{1}{\Gamma}\right)\right] \Big/ \widehat{\left(\frac{1}{\Gamma}\right)}^{2}$$

is satisfied approximately. With that we set $\hat{p} = \widehat{(p/\Gamma)}/\widehat{(1/\Gamma)}$ and $\hat{\Gamma} = 1/\widehat{(1/\Gamma)}$. To finish the construction of $\hat{A}(q_L, q_R)$, we still need to find the averages of $\mathcal{B}$ and $\chi$. Since there is no unique way to do so, we might as well compute $\hat{\mathcal{B}}$ and $\hat{a}$ using (28) and set $\hat{\chi} = [(2/\hat{\Gamma}) - 2 - \hat{\varphi}\hat{\rho}]\hat{a}\hat{\rho}$, where $\hat{\rho} = \sqrt{\rho_L \rho_R}$. Numerical results shown in Section 3.4 indicate that the set of average states described here is a good one to use for practical multicomponent problems.

The solution of the linear problem (26) consists of eight discontinuities propagating at constant speeds (for a system of eight equations). The jump across each discontinuity is a multiple of the eigenvector of the matrix $\hat{A}$, and the propagating speed is the corresponding eigenvalue. We thus have

$$\Delta q = q_R - q_L = \sum_{k=1}^{8} \hat{\alpha}_k \hat{r}_k, \tag{29}$$

where $\hat{r}_k$ is the $k$th eigenvector of $\hat{A}$; see (16a) and (16b). The scalar $\hat{\alpha}_k$ gives the strength across the discontinuity that can be determined easily from (29). We find

$$\begin{aligned}
\hat{\alpha}_2 &= \Delta q^{(1)} + \frac{\hat{\Gamma}}{\hat{c}^2}\left[-\frac{\hat{u}^2}{2}\Delta q^{(1)} + \hat{u}\Delta q^{(2)} - \Delta q^{(3)} + \hat{p}\left(\Delta q^{(7)} - \Delta q^{(4)}\right) + \Delta q^{(5)} + \Delta q^{(6)}\right],\\
\hat{\alpha}_3 &= \frac{1}{2\hat{c}}\left[(\hat{c} - \hat{u})\Delta q^{(1)} + \Delta q^{(2)} - \hat{c}\hat{\alpha}_2\right],\\
\hat{\alpha}_1 &= \Delta q^{(1)} - \hat{\alpha}_2 - \hat{\alpha}_3, \qquad \hat{\alpha}_4 = \Delta q^{(4)} - \hat{\varphi}(\Delta\rho - \hat{\alpha}_2),\\
\hat{\alpha}_5 &= \Delta q^{(5)} - \hat{\varphi}\hat{\mathcal{B}}(\Delta\rho - \hat{\alpha}_2), \quad \hat{\alpha}_6 = \Delta q^{(6)} - \hat{\chi}(\Delta\rho - \hat{\alpha}_2),\\
\hat{\alpha}_7 &= \Delta q^{(7)}, \qquad \hat{\alpha}_8 = \Delta q^{(8)},
\end{aligned} \tag{30}$$

where $\hat{c} = \sqrt{\hat{\Gamma}[\hat{H} - (\hat{u}^2/2) + \hat{p}\hat{\varphi} - \hat{\varphi}\hat{\mathcal{B}} - \hat{\chi}]}$ is the speed of sound.

Note that in this Riemann solution, except the discontinuities for $\hat{\lambda}_1 = \hat{u} - \hat{c}$, and $\hat{\lambda}_3 = \hat{u} + \hat{c}$, all the other discontinuities (six of them) are propagating at the same speed $\hat{u}$. For practical purposes, we may view these discontinuities as a single one with the operator $\mathcal{W}_2$ defined by combining all the jumps across the $\hat{\lambda}_2$ wave family; i.e., set $\mathcal{W}_2 = \hat{\alpha}_2\hat{r}_2 + \sum_{k=4}^{8} \hat{\alpha}_k\hat{r}_k$. Clearly, doing so removes the effect of the wave families $\hat{\lambda}_4$ to $\hat{\lambda}_8$ from the solution. With this notation, we also write $\mathcal{W}_k = \hat{\alpha}_k\hat{r}_k$ to represent the jump across the $k$-wave for $k = 1$ or 3.

### 3.3. *Wave Propagation Methods*

We use the high-resolution method based on a wave-propagation viewpoint to compute approximate solutions of our multicomponent model introduced in Section 3.1. The method is a variant of the fluctuation-and-signal scheme of Roe [58, 59] in that we solve the Riemann

problems at each cell interface and use the resulting waves (i.e., discontinuities moving at constant speeds) to update the solutions in neighboring grid cells (cf. [34, 39]).

For simlicity, we describe the method on a uniform grid with fixed mesh spacing $\Delta x$, but the method can be extended quite easily to a nonuniform and time-varying grid as well (cf. [35, 40]). We use a standard finite-volume formulation in which the value $Q_j^n$ approximates the cell average of the solution over the grid cell $[x_j, x_{j+1}]$ at time $t_n$:

$$Q_j^n \approx \frac{1}{\Delta x} \int_{x_j}^{x_{j+1}} q(x, t_n)\, dx.$$

The time step from the current time $t_n$ to the next $t_{n+1}$ is denoted by $\Delta t$.

*3.3.1. First order method.* In this setup, a first order accurate version of the method in wave-propagation form is a Godunov-type scheme that can be written as

$$Q_j^{n+1} = Q_j^n - \frac{\Delta t}{\Delta x} \sum_{k=1}^{m_w} (\lambda_k^- \mathcal{W}_k)_{j+1}^n + (\lambda_k^+ \mathcal{W}_k)_j^n, \tag{31}$$

where $\lambda_k \in \mathbb{R}$ and $\mathcal{W}_k \in \mathbb{R}^m$ are solutions of the $k$th wave family, for $k = 1, 2, \ldots, m_w$, obtained from solving the Riemann problems at cell interfaces $x_j$ and $x_{j+1}$, $\lambda^- = \min(\lambda, 0)$, and $\lambda^+ = \max(\lambda, 0)$. Clearly, the method belongs to a class of upwind schemes (cf. [23, 36]), and it will be shown next that the method is quasi-conservative in the sense that when applying the method to (13) not only the conservation equations but also the transport equations are approximated in a consistent manner by the method with the chosen Riemann solver.

To demonstrate that, we first analyze our method for an interface only problem as described in Section 3.1. Without loss of generality, we consider a single Riemann problem where at cell interface $x_j$ the initial data consists of uniform pressure $p_0$ and constant particle velocity $u_0$ to the left and right of the interface, but with jumps on the other state variables of $q$. Assuming a positive velocity $u_0 > 0$, for example. If the problem is solved by using a shock-only Riemann solver (see Section 3.2.1), from (31) the cell average $Q_j^n$ would be updated by

$$Q_j^{n+1} = Q_j^n - \frac{\Delta t}{\Delta x} (\lambda_2 \mathcal{W}_2)_j^n, \tag{32a}$$

or equivalently by

$$\begin{bmatrix} \rho \\ \rho u \\ \rho E \\ \frac{b\rho}{\gamma - 1} \\ \frac{\gamma - b\rho}{\gamma - 1}\mathcal{B} \\ \frac{2 - \gamma - b\rho}{\gamma - 1} a\rho^2 \\ \frac{1}{\gamma - 1} \\ a \end{bmatrix}_j^{n+1} = \begin{bmatrix} \rho \\ \rho u_0 \\ \rho E \\ \frac{b\rho}{\gamma - 1} \\ \frac{\gamma - b\rho}{\gamma - 1}\mathcal{B} \\ \frac{2 - \gamma - b\rho}{\gamma - 1} a\rho^2 \\ \frac{1}{\gamma - 1} \\ a \end{bmatrix}_j^{n} - \frac{\Delta t}{\Delta x} u_0 \begin{bmatrix} \Delta\rho \\ u_0 \Delta\rho \\ \Delta\rho E \\ \Delta\frac{b\rho}{\gamma - 1} \\ \Delta\frac{\gamma - b\rho}{\gamma - 1}\mathcal{B} \\ \Delta\frac{2 - \gamma - b\rho}{\gamma - 1} a\rho^2 \\ \Delta\frac{1}{\gamma - 1} \\ \Delta a \end{bmatrix}_j^{n}, \tag{32b}$$

when expressing (32a) in terms of the solution states of the problem. Noting that in this case the difference operator $\Delta$ is simply applied to the Riemann data $Q_{j-1}^n$ and $Q_j^n$ on

the left and right of the interface. With this, from the first two equations of (32b), we find the expected state of the particle velocity $u_j^{n+1} = u_0$. Employing the updates from (32b) to (14) yields quite easily the desired pressure equilibrium $p_j^{n+1} = p_0$ at the $j$th cell; see [63] for a different way to derive the same result. As to the behavior of the other state variables, it is not difficult to show monotonicity of the solutions when the usual CFL (Courant–Friedrichs–Lewy) condition for stability of the method is satisfied (cf. [36]).

Note that alternatively if the Roe approximate solver (see Section 3.2.2) is used to solve the problem, from (30) we find the strength across the waves as

$$(\hat{\alpha}_1, \hat{\alpha}_2, \ldots, \hat{\alpha}_8)_j^n = \left(0, \Delta\rho, 0, \Delta\frac{b\rho}{\gamma-1}, \Delta\frac{\gamma-b\rho}{\gamma-1}\mathcal{B}, \Delta\frac{2-\gamma-b\rho}{\gamma-1}a\rho^2, \Delta\frac{1}{\gamma-1}, \Delta a\right)_j^n.$$

While from our averaging procedure, we obtain the correct average states for $\hat{u}_j^n = u_0$ and $\hat{p}_j^n = p_0$. Combining all these with the eigenvectors $\{\hat{r}_k\}$ defined in an average state produces the only nonzero jump across the 2-wave,

$$\mathcal{W}_2 = \hat{\alpha}_2\hat{r}_2 + \sum_{k=4}^{8}\hat{\alpha}_k\hat{r}_k = \left(\Delta\rho, u_0\Delta\rho, \frac{u_0^2}{2}\Delta\rho + p_0\Delta\frac{1-b\rho}{\gamma-1} + \Delta\frac{\gamma-b\rho}{\gamma-1}\mathcal{B}\right.$$
$$\left. + \Delta\frac{2-\gamma-b\rho}{\gamma-1}a\rho^2, \Delta\frac{b\rho}{\gamma-1}, \Delta\frac{\gamma-b\rho}{\gamma-1}\mathcal{B}, \Delta\frac{2-\gamma-b\rho}{\gamma-1}a\rho^2, \Delta\frac{1}{\gamma-1}, \Delta a\right)^T,$$

with the propagating speed $\lambda_2 = u_0$. Not surprisingly, we get the exact Riemann problem solution as presented in (32b) and hence the same numerical result for this interface only problem by using the Roe solver. Without causing any ambiguity, we have dropped the superscript $n$ and subscript $j$ for simplifying the above expression.

We next discuss how our method works when there are some other waves coming into the $j$th cell and affecting the cell average $Q_j^{n+1}$ also. As an example, suppose that we are taking Riemann data at cell interface $x_{j+1}$ so that the solution consists of a 1-wave (shock or rarefaction) propagating to the left of the interface. In this method, from (32a) the cell average $Q_j^{n+1}$ should be further updated by

$$Q_j^{n+1} := Q_j^{n+1} - \frac{\Delta t}{\Delta x}(\lambda_1\mathcal{W}_1)_{j+1}^n, \tag{33a}$$

where the Riemann problem solution $\lambda_1$ and $\mathcal{W}_1$ may be computed by using either the shock-only or Roe solver as mentioned before.

Considering a case with the Roe solver, for instance, (33a) then takes the form

$$\begin{bmatrix} \rho \\ \rho u \\ \rho E \\ \frac{b\rho}{\gamma-1} \\ \frac{\gamma-b\rho}{\gamma-1}\mathcal{B} \\ \frac{2-\gamma-b\rho}{\gamma-1}a\rho^2 \\ \frac{1}{\gamma-1} \\ a \end{bmatrix}_j^{n+1} := \begin{bmatrix} \rho \\ \rho u \\ \rho E \\ \frac{b\rho}{\gamma-1} \\ \frac{\gamma-b\rho}{\gamma-1}\mathcal{B} \\ \frac{2-\gamma-b\rho}{\gamma-1}a\rho^2 \\ \frac{1}{\gamma-1} \\ a \end{bmatrix}_j^{n+1} - \frac{\Delta t}{\Delta x}(\hat{u}-\hat{c})_{j+1}^n \begin{bmatrix} \hat{\alpha}_1 \\ \hat{\alpha}_1(\hat{u}-\hat{c}) \\ \hat{\alpha}_1(\hat{H}-\hat{u}\hat{c}) \\ \hat{\alpha}_1\hat{\varphi} \\ \hat{\alpha}_1\hat{\varphi}\hat{\mathcal{B}} \\ \hat{\alpha}_1\hat{\chi} \\ 0 \\ 0 \end{bmatrix}_{j+1}^n. \tag{33b}$$

It is interesting to note that, due to a fundamental property of the Roe solver, i.e., the relation in (27), this is a conservative update of the first four components of (33b). Clearly, from the last two components, the quantities $\gamma$ and $a$ are not affected by the propagation of the 1-wave. Substituting the mass-conservation update $\rho_j^{n+1}$ into the fourth and fifth components of (33b), after a simple manipulation, we find the quantities $b$ and $\mathcal{B}$ remain unchanged as well; this is a result we expect and is true irrespective of any reasonable choice of $\hat{\mathcal{B}}$ (for example, the Roe-averaging of $\mathcal{B}$ discussed in Section 3.2.2). We use the update of $a\rho^2(2-\gamma-b\rho)/(\gamma-1)$ primarily to the computation of the pressure from the equation of state (14), and so the choice of $\hat{\chi}$ does not affect the quantity $a$ in a direct manner.

In summary, it should be clear that (31) is a consistent approximation of our quasi-conservative model (13). Concerning stability, it is observed numerically that the method is stable and convergent under mesh refinement provided that the waves in the method affect only the cells adjacent to the interface during the time step. One advantage of using the wave-propagation form is that we are able to handle each wave in turn, and there is no need to compute fluxes and make a distinction between the waves. Extension of the method to higher order accuracy, and in particular to a high-resolution version of the wave propagation scheme, follows easily as will be described next.

*3.3.2. High resolution corrections.* To achieve high resolution in a wave-propagation method, we begin by introducing correction waves in a piecewise-linear form with zero mean value. We then propagate each wave over the time step $\Delta t$ and update the cell averages it overlaps. Without going into the details here (cf. [40]), with the corrections, (31) is modified by

$$Q_j^{n+1} := Q_j^{n+1} - \frac{\Delta t}{2\Delta x}\sum_{k=1}^{m_w}\left[|\lambda_k|\left(1-|\lambda_k|\frac{\Delta t}{\Delta x}\right)\mathcal{W}_k\right]_{j+1}^{n} - \left[|\lambda_k|\left(1-|\lambda_k|\frac{\Delta t}{\Delta x}\right)\mathcal{W}_k\right]_{j}^{n}. \quad (34)$$

It is important to mention that, in practice, the strength of each wave should be limited by using a "slope-limiter" to avoid unnecessary fluctuations near discontinuities. We want to do this by replacing each $\mathcal{W}_k$ in (34) with a limited value $\widetilde{\mathcal{W}}_k$ obtained by comparing $\mathcal{W}_k$ with the corresponding $\mathcal{W}_k$ from the neighboring Riemann problem to the left (if $\lambda_k > 0$) or to the right (if $\lambda_k < 0$).

Suppose that we are using the Roe solver to the computations; it is quite common to limit over each strength of the wave $\hat{\alpha}_{kj}$ via a limiter function $\phi$ (e.g., by using the minmod function $\phi(\theta) = \max(0, \min(1, \theta))$ or some others as discussed in [70]) and set

$$\tilde{\alpha}_{kj} = \phi(\theta_{kj})\hat{\alpha}_{kj} \quad \text{with} \quad \theta_{kj} = \frac{\hat{\alpha}_{kJ}}{\hat{\alpha}_{kj}}, \quad J = \begin{cases} j-1 & \text{if } \hat{\lambda}_{kj} \geq 0 \\ j+1 & \text{if } \hat{\lambda}_{kj} < 0, \end{cases} \quad (35)$$

for $k = 1, 2, \ldots, 8$ (cf. [23, 37, 39]). In this approach, we then replace the waves in (34),

$$(\mathcal{W}_1, \mathcal{W}_2, \mathcal{W}_3) = \left(\hat{\alpha}_1\hat{r}_1, \hat{\alpha}_2\hat{r}_2 + \sum_{k=4}^{8}\hat{\alpha}_k\hat{r}_k, \hat{\alpha}_3\hat{r}_3\right),$$

by a limited version as

$$(\widetilde{\mathcal{W}}_1, \widetilde{\mathcal{W}}_2, \widetilde{\mathcal{W}}_3) = \left(\tilde{\alpha}_1\hat{r}_1, \tilde{\alpha}_2\hat{r}_2 + \sum_{k=4}^{8}\hat{\alpha}_k\hat{r}_k, \tilde{\alpha}_3\hat{r}_3\right).$$

It is not difficult to show that for the interface only problem we again have the required pressure equilibrium that is independent of the limiter being employed to the high-resolution method (34). Moreover, we obtain a better resolution of the result as compared to the first order result.

Note that if the shock-only solver is employed to the computations, analogously to (35), we may apply a slope limiter separately to each component of the waves, i.e.,

$$\widetilde{\mathcal{W}}_{kj}^{(i)} = \phi\big(\theta_{kj}^{(i)}\big)\mathcal{W}_{kj}^{(i)} \quad \text{with} \quad \theta_{kj}^{(i)} = \frac{\mathcal{W}_{kJ}^{(i)}}{\mathcal{W}_{kj}^{(i)}}, \quad J = \begin{cases} j-1 & \text{if } \lambda_{kj} \geq 0 \\ j+1 & \text{if } \lambda_{kj} < 0, \end{cases}$$

where $\mathcal{W}_{kj}^{(i)}$ is the $i$th component of $\mathcal{W}_{kj}$, for $k = 1, 2, 3$, and $i = 1, 2, \ldots, 8$. While this approach works quite well for the 1- and 3-waves, for the 2-wave, however, in some cases because of the sixfold eigenvalue degeneracy, it requires a slight modification of the third limited component on the total energy $\widetilde{\mathcal{W}}_{kj}^{(3)}$ so as to ensure a consistent approximation of that term. Motivated by the treatment of the 2-wave in the Roe solver, this may be done by setting

$$\widetilde{\mathcal{W}}_{2j}^{(3)} = \frac{u_{*j}^2}{2}\widetilde{\mathcal{W}}_{2j}^{(1)} + p_{*j}\big(\widetilde{\mathcal{W}}_{2j}^{(7)} - \widetilde{\mathcal{W}}_{2j}^{(4)}\big) + \widetilde{\mathcal{W}}_{2j}^{(5)} + \widetilde{\mathcal{W}}_{2j}^{(6)},$$

where $u_{*j}$ and $p_{*j}$ are solutions of the Riemann problem at cell interface $x_j$. With the limited waves, we again observe good results obtained using the high-resolution method with the shock-only Riemann solver.

### 3.4. *Numerical Results*

We now present results to validate our multicomponent algorithm described in Section 3.3.

EXAMPLE 3.4.1. As a first example, we consider an interface only problem where the solution of a Riemann problem consists of a single contact discontinuity evolving in a liquid with uniform equilibrium pressure $p_0 = 10^5$ Pa and constant particle velocity $u_0 = 10^3$ m/s. Initially, the interface is located at $x = 0.2$ m of a shock tube of unit length. On the left of the interface, the fluid is a gas with

$$(\rho, \gamma, a, b)_L = (50 \ \text{kg/m}^3, 1.4, 10^{-3} \ \text{m}^3/\text{kg}, 5 \ \text{Pa m}^6/\text{kg}),$$

while on the right of the interface, the fluid is a liquid with

$$(\rho, \gamma, \mathcal{B})_R = (10^3 \ \text{kg/m}^3, 4.4, 6 \times 10^8 \ \text{Pa}).$$

Calculations were carried out by using the high-resolution version of the method with a 200 grid, the Roe solver, and the "minmod" limiter [36]. After 210 time steps (time $t = 360$ $\mu$s and Courant number 0.9 approximately), we obtain the results shown in Fig. 3. Notice that the pressure and also the particle velocity remain at the correct constant states $p_0$ and $u_0$, respectively, without any spurious oscillations near the interface. Comparing with the exact solution, the other variables such as $\rho$, $T$, $\gamma$, $a$, $b$, and $\mathcal{B}$ behave in a satisfactory manner as well.

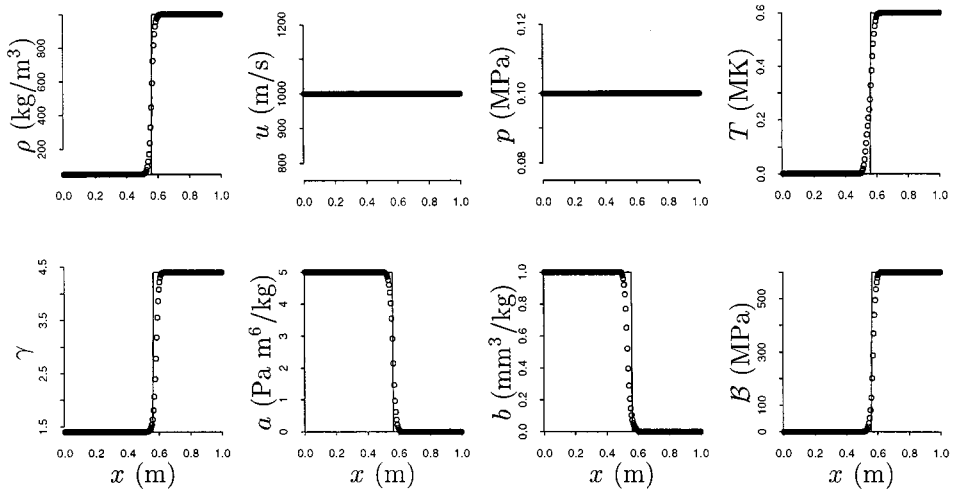


**FIG. 3.** High-resolution results for an interface only problem at time $t = 360$ $\mu$s. The solid line is the exact solution and the points show the computed solution with 200 mesh points.

EXAMPLE 3.4.2. Our next example is concerned with a more general two-phase liquid–gas Riemann problem. In this case, the initial condition consists of two constant states with data

$$(\rho, u, p) = \begin{cases} (10^3 \text{ kg/m}^3, 0 \text{ m/s}, 10^9 \text{ Pa}) & \text{for } x \le 0.7 \text{ m} \\ (50 \text{ kg/m}^3, 0 \text{ m/s}, 10^5 \text{ Pa}) & \text{for } x > 0.7 \text{ m}, \end{cases}$$

where on the left we have the liquid phase with $\gamma = 4.4$ and $\mathcal{B} = 6 \times 10^8$ Pa, and on the right we have the gas phase with $\gamma = 1.4$, $a = 5$ Pa m$^6$/kg, and $b = 10^{-3}$ m$^3$/kg. Breaking of the liquid–gas membrane results in a leftward going rarefaction wave, a rightward going contact discontinuity, and a shock wave.

As in Example 3.4.1, we run the problem in a shock tube using the same high-resolution method, but with a 500 grid for checking convergence of the results. Since the solution of this Riemann problem is self-similar in the $x$–$t$ plane, in Fig. 4, we only show results at a single stopping time, $t = 240$ $\mu$s. Observing the displayed profiles, we clearly obtain the correct behavior of the computed contact discontinuity and also the shock and rarefaction waves as in comparison with the exact solution. At the tail of the rarefaction wave, the slight overshoot of the particle velocity and also the undershoot of the pressure are typical numerical artifacts when the Roe approximate solver is used to the computation; this includes the case for single component problems also. Numerical evidences suggest, however, that these errors decrease as the mesh is refined with a rate proportional to the order of accuracy of the method. It should be noted that the aforementioned errors near the rarefaction wave are often not visible when the shock-only Riemann solver is employed instead (not shown here); see [60] for an example.

EXAMPLE 3.4.3. To show how our algorithm performs on shock-contact interactions, we consider a model problem in which the initial condition is composed of a stationary interface at $x = 0.4$ m and a leftward going Mach 1.422 shock wave at $x = 0.5$ m traveling from right to left (cf. [1, 30, 63] for a similar test). The fluid on the left of the interface is a

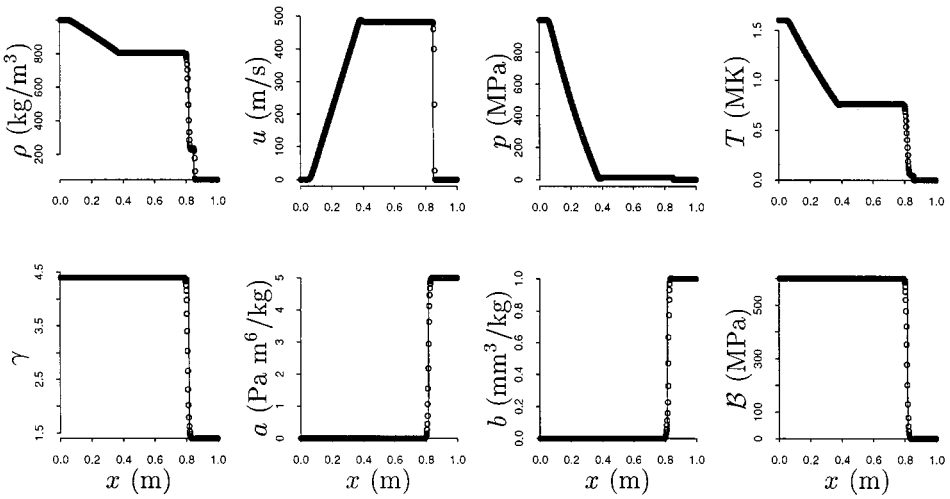


**FIG. 4.** High-resolution results for a two-phase liquid–gas Riemann problem at time $t = 240$ $\mu$s. The solid line is the exact solution and the points show the computed solution with 500 mesh points.

van der Waals gas with

$$(\rho,\, p,\, \gamma,\, a,\, b)_L = (1.2 \text{ kg/m}^3,\, 10^5 \text{ Pa},\, 1.4,\, 10^{-3} \text{ m}^3/\text{kg},\, 5 \text{ Pa m}^6/\text{kg}),$$

and the fluid on the right of the interface (i.e., on the middle and the preshock state) is a liquid with

$$(\rho,\, p,\, \gamma,\, \mathcal{B})_M = (10^3 \text{ kg/m}^3,\, 10^5 \text{ Pa},\, 4.4,\, 6 \times 10^8 \text{ Pa}).$$

The state behind the shock is

$$(\rho, u,\, p)_R = (1.23 \times 10^3 \text{ kg/m}^3,\, -432.69 \text{ m/s},\, 10^9 \text{ Pa});$$

see the dashed line shown in Fig. 5 for illustration. We note that this gives us one example, in which the interface is accelerated by a shock wave coming from the heavy-fluid to the light-fluid region, and the resulting wave pattern after the interaction would consist of a transmitted shock wave, an interface, and a reflected rarefaction wave (cf. Fig. 4 of [63]).

For this problem, snapshots of the computed solutions are shown in Fig. 5 at time $t = 270$ $\mu$s, where we again solve the problem using the high-resolution method with 500 mesh points. From the plots of $\rho, u$, and $p$, it is clear that the shock wave and contact discontinuity are very well located, and the rarefaction wave moves at the correct speed with the correct shape also. There are some postshock undershoots of the temperature $T$ in the front of the interface, however. Results of numerous experiments point to the fact that this type of error is inherent in any shock wave computation (in fact, the stronger the incoming shock wave is, the larger the undershoot is) when a shock-capturing method is employed for approximating the interaction between shocks and interfaces (cf. [2] for a related issue on postshock oscillations).

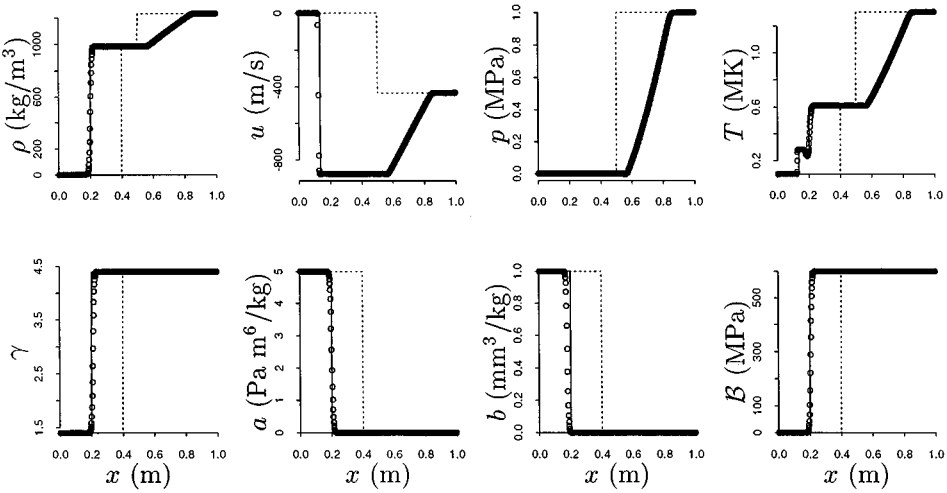


**FIG. 5.** High-resolution results for a shock-contact interaction problem at time $t = 270$ $\mu$s. The solid line is the exact solution and the points shows the computed solution with 500 mesh points. The dashed line in each subplot is the initial condition at time $t = 0$.

## 4. TWO SPACE DIMENSIONS

We now discuss the generalization of our one-dimensional multicomponent algorithm to multiple space dimensions. For simplicity, we focus our discussion on two-dimensional problems, but much of the same idea described here can be extended in a straightforward manner to three space dimensions as well.

### 4.1. *Model Equations*

Following the same development as introduced in Section 3.1, the two-dimensional version of the model (13) for compressible multicomponent problems with the modified van der Waals equation of state (5) takes the form

$$
\begin{cases}
\partial_t \rho + \partial_x(\rho u) + \partial_y(\rho v) = 0 \\
\partial_t(\rho u) + \partial_x(\rho u^2 + p) + \partial_y(\rho u v) = 0 \\
\partial_t(\rho u) + \partial_x(\rho u v) + \partial_y(\rho v^2 + p) = 0 \\
\partial_t(\rho E) + \partial_x(\rho E u + p u) + \partial_y(\rho E v + p v) = 0 \\
\partial_t\left(\frac{b\rho}{\gamma-1}\right) + \partial_x\left(\frac{b\rho}{\gamma-1}u\right) + \partial_y\left(\frac{b\rho}{\gamma-1}v\right) = 0 \\
\partial_t\left(\frac{\gamma-b\rho}{\gamma-1}\mathcal{B}\right) + \partial_x\left(\frac{\gamma-b\rho}{\gamma-1}\mathcal{B}u\right) + \partial_y\left(\frac{\gamma-b\rho}{\gamma-1}\mathcal{B}v\right) = \left(\frac{\gamma}{\gamma-1}\mathcal{B}\right)(\partial_x u + \partial_y v) \\
\partial_t\left(\frac{2-\gamma-b\rho}{\gamma-1}a\rho^2\right) + \partial_x\left(\frac{2-\gamma-b\rho}{\gamma-1}a\rho^2 u\right) + \partial_y\left(\frac{2-\gamma-b\rho}{\gamma-1}a\rho^2 v\right) \\
\quad = -\left(\frac{2-\gamma-2b\rho}{\gamma-1}a\rho^2\right)(\partial_x u + \partial_y v) \\
\partial_t\left(\frac{1}{\gamma-1}\right) + u\partial_x\left(\frac{1}{\gamma-1}\right) + v\partial_y\left(\frac{1}{\gamma-1}\right) = 0 \\
\partial_t a + u\partial_x a + v\partial_y a = 0.
\end{cases}
\tag{36}
$$

Clearly, in the model, the first four components are the Euler Eqs. (1) for the basic conservative fluid mixtures $\rho$, $\rho u$, $\rho v$, and $\rho E$, while the remaining ones are the effective equations

for the problem-dependent material quantities. As in the one-dimensional case, we take the effective equations to be of the form that is viable for numerical approximation and may therefore set the pressure from the equation of state,

$$p = \left[\rho E - \frac{(\rho u)^2 + (\rho v)^2}{2\rho} - \left(\frac{\gamma - b\rho}{\gamma - 1}\mathcal{B}\right) - \left(\frac{2 - \gamma - b\rho}{\gamma - 1} a\rho^2\right)\right] \Big/ \left(\frac{1 - b\rho}{\gamma - 1}\right). \quad (37)$$

Note again that the model has been formulated in such a way that it reduces to the usual Euler Eqs. (1) for a single component flow.

To examine the basic solution structure of this two-dimensional model, it is instructive to write (36) in a quasi-linear system of equations

$$\partial_t q + A(q)\partial_x q + B(q)\partial_y q = 0 \quad (38)$$

with the state vector $q$ defined by

$$q = \left[\rho, \rho u, \rho v, \rho E, \frac{b\rho}{\gamma - 1}, \frac{\gamma - b\rho}{\gamma - 1}\mathcal{B}, \frac{2 - \gamma - b\rho}{\gamma - 1} a\rho^2, \frac{1}{\gamma - 1}, a\right]^T$$

and the matrices $A$ and $B$ given by

$$A(q) = \begin{bmatrix} 0 & 1 & 0 & 0 & 0 & 0 & 0 & 0 & 0 \\ K - u^2 & u(2 - \Gamma) & -v\Gamma & \Gamma & p\Gamma & -\Gamma & -\Gamma & -p\Gamma & 0 \\ -uv & v & u & 0 & 0 & 0 & 0 & 0 & 0 \\ u(K - H) & H - u^2\Gamma & -uv\Gamma & u(\Gamma + 1) & up\Gamma & -u\Gamma & -u\Gamma & -up\Gamma & 0 \\ -\varphi u & \varphi & 0 & 0 & u & 0 & 0 & 0 & 0 \\ \varphi u\mathcal{B} & -\varphi\mathcal{B} & 0 & 0 & 0 & u & 0 & 0 & 0 \\ -\chi u & \chi & 0 & 0 & 0 & 0 & u & 0 & 0 \\ 0 & 0 & 0 & 0 & 0 & 0 & 0 & u & 0 \\ 0 & 0 & 0 & 0 & 0 & 0 & 0 & 0 & u \end{bmatrix}$$

and

$$B(q) = \begin{bmatrix} 0 & 0 & 1 & 0 & 0 & 0 & 0 & 0 & 0 \\ -uv & u & u & 0 & 0 & 0 & 0 & 0 & 0 \\ K - v^2 & -u\Gamma & v(2 - \Gamma) & \Gamma & p\Gamma & -\Gamma & -\Gamma & -p\Gamma & 0 \\ v(K - H) & -uv\Gamma & H - v^2\Gamma & v(\Gamma + 1) & vp\Gamma & -v\Gamma & -v\Gamma & -vp\Gamma & 0 \\ -\varphi v & 0 & \varphi & 0 & v & 0 & 0 & 0 & 0 \\ \varphi v\mathcal{B} & 0 & -\varphi\mathcal{B} & 0 & 0 & v & 0 & 0 & 0 \\ -\chi v & 0 & \chi & 0 & 0 & 0 & v & 0 & 0 \\ 0 & 0 & 0 & 0 & 0 & 0 & 0 & v & 0 \\ 0 & 0 & 0 & 0 & 0 & 0 & 0 & 0 & v \end{bmatrix}.$$

Recall that $\Gamma$, $H$, $\varphi$, and $\chi$ represent the same physical quantities as those described in Section 3.1, and here $K = \Gamma(u^2 + v^2)/2$. It is easy to show that the spectrum of the matrices $A$ and $B$ are

$$\Lambda_A = \mathrm{diag}(\lambda_1, \lambda_2, \ldots, \lambda_9) = \mathrm{diag}(u - c, u, u + c, u, \ldots, u)$$

and

$$\Lambda_B = \mathrm{diag}(\mu_1, \mu_2, \ldots, \mu_9) = \mathrm{diag}(v - c, v, v + c, v, \ldots, v),$$

respectively, with the corresponding set of eigenvectors

$$R_A = (r_1, r_2, \ldots, r_9) = \begin{bmatrix} 1 & 1 & 1 & 0 & 0 & 0 & 0 & 0 & 0 \\ u - c & u & u + c & 0 & 0 & 0 & 0 & 0 & 0 \\ v & v & v & 1 & 0 & 0 & 0 & 0 & 0 \\ H - uc & \frac{1}{2}(u^2 + v^2) & H + uc & v & -p & 1 & 1 & p & 0 \\ \varphi & 0 & \varphi & 0 & 1 & 0 & 0 & 0 & 0 \\ \varphi\mathcal{B} & 0 & \varphi\mathcal{B} & 0 & 0 & 1 & 0 & 0 & 0 \\ \chi & 0 & \chi & 0 & 0 & 0 & 1 & 0 & 0 \\ 0 & 0 & 0 & 0 & 0 & 0 & 0 & 1 & 0 \\ 0 & 0 & 0 & 0 & 0 & 0 & 0 & 0 & 1 \end{bmatrix}$$

and

$$R_B = (\omega_1, \omega_2, \ldots, \omega_9) = \begin{bmatrix} 1 & 1 & 1 & 0 & 0 & 0 & 0 & 0 & 0 \\ u & u & u & 1 & 0 & 0 & 0 & 0 & 0 \\ v - c & v & v + c & 0 & 0 & 0 & 0 & 0 & 0 \\ H - vc & \frac{1}{2}(u^2 + v^2) & H + vc & u & -p & 1 & 1 & p & 0 \\ \varphi & 0 & \varphi & 0 & 1 & 0 & 0 & 0 & 0 \\ \varphi\mathcal{B} & 0 & \varphi\mathcal{B} & 0 & 0 & 1 & 0 & 0 & 0 \\ \chi & 0 & \chi & 0 & 0 & 0 & 1 & 0 & 0 \\ 0 & 0 & 0 & 0 & 0 & 0 & 0 & 1 & 0 \\ 0 & 0 & 0 & 0 & 0 & 0 & 0 & 0 & 1 \end{bmatrix},$$

where $Ar_k = \lambda_k r_k$ and $B\omega_k = \mu_k \omega_k$. With this, it is sufficient to conclude that (38), and hence (36), are hyperbolic in the sense that any linear combination of the matrices $A$ and $B$ given above is assumed to have real eigenvalues and a complete set of eigenvectors for each physically relevant value of the state variables $q$ located in the region of thermodynamic stability.

For the convenience of the latter reference, we write (36) to a more compact expression by

$$\partial_t q + f(\partial_x, q) + g(\partial_y, q) = 0 \tag{39}$$

with $f$ and $g$ taken to be the vector-value functions of the following form:

$$f = \Bigg[\partial_x(\rho u), \partial_x(\rho u^2 + p), \partial_x(\rho u v), \partial_x(\rho E u + p u), \partial_x\left(\frac{b\rho}{\gamma - 1}u\right),$$
$$\partial_x\left(\frac{\gamma - b\rho}{\gamma - 1}\mathcal{B}\right) - \left(\frac{\gamma\mathcal{B}}{\gamma - 1}\right)\partial_x u, \partial_x\left(\frac{2 - \gamma - b\rho}{\gamma - 1}a\rho^2 u\right) + \left(\frac{2 - \gamma - 2b\rho}{\gamma - 1}a\rho^2\right)\partial_x u,$$
$$u\partial_x\left(\frac{1}{\gamma - 1}\right), u\partial_x a\Bigg]^T$$

and

$$g = \left[\partial_y(\rho v),\ \partial_y(\rho uv),\ \partial_y(\rho v^2 + p),\ \partial_y(\rho Ev + pv),\ \partial_y\left(\frac{b\rho}{\gamma - 1}v\right),\right.$$
$$\partial_y\left(\frac{\gamma - b\rho}{\gamma - 1}\mathcal{B}\right) - \left(\frac{\gamma\mathcal{B}}{\gamma - 1}\right)\partial_y v,\ \partial_y\left(\frac{2 - \gamma - b\rho}{\gamma - 1}a\rho^2 v\right) + \left(\frac{2 - \gamma - 2b\rho}{\gamma - 1}a\rho^2\right)\partial_y v,$$
$$\left.v\partial_y\left(\frac{1}{\gamma - 1}\right),\ v\partial_y a\right]^T.$$

Clearly, the functions $f$ and $g$ defined above reduce to the standard flux functions for a single component flow.

### 4.2. *Wave Propagation Methods*

To compute approximate solutions of (36) numerically for practical multicomponent problems, we employ a two-dimensional generalization of the high-resolution wave propagation method. In this method, waves obtained from solving one-dimensional Riemann problems in the directions normal and tangential to each cell interface are used to update the solutions in neighboring cells. As in the one-dimensional case, see Section 3.3.2, we introduce slopes and limiters to achieve a high resolution of results.

For simplicity, we describe the method on a uniform Cartesian grid with fixed mesh spacing $\Delta x$ and $\Delta y$ in the $x$- and $y$-direction, respectively; see [35, 41] for a more general discussion of the method when applied to an unstructure and time-varying grid. As before, we use a finite-volume formulation in which the value $Q_{ij}^n$ approximates the cell average of the solution over the $(i, j)$th grid cell at time $t_n$,

$$Q_{ij}^n \approx \frac{1}{\Delta x \Delta y}\int_{\Omega_{ij}} q(x, y, t_n)\, dx\, dy.$$

Here $\Omega_{ij}$ denotes the rectangular region occupied by the grid cell $(i, j)$.

*4.2.1. First order method.* To demonstrate the basic idea, consider the interface between cells $(i - 1, j)$ and $(i, j)$ as illustrated in Fig. 6, for example. We solve the one-dimensional

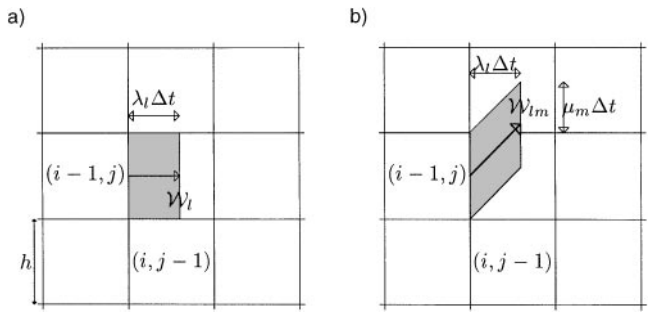


**FIG. 6.** First order wave propagation method. (a) Normal wave propagation, a case with the Riemann problem solution in the $x$-direction is shown, $\lambda_l > 0$. (b) Transverse wave propagation, a case with the splitting of the $l$th wave shown in (a) in the $y$-direction. Only the $m$th subwave is plotted, $\mu_m > 0$. The cell averages affected by the shaded region of the wave are updated. Note for convenience we have drawn the graph with $\Delta x = \Delta y = h$.

Riemann problem normal to this face, which in this case will be

$$\partial_t q + f(\partial_x, q) = 0,$$

with initial data given by $Q^n_{i-1,j}$ and $Q^n_{ij}$. If we use the shock-only Riemann solver as described in Section 3.2.1, we again find the solution consisting of three discontinuities propagating at constant speeds, and the jump across each discontinuity is the difference between the state variables to the left and right of the discontinuity; see Fig. 2 for the typical structure of the solution and (25a) and (25b) for the mathematical expression of the solutions. Note that in the current case of the Riemann problem solution the particle velocity in the $y$-direction is advanced in a passive manner along the $\lambda_2$ family (cf. [23]). With this type of Riemann solver we have the usual splitting of jumps into waves:

$$\Delta q = Q^n_{ij} - Q^n_{i-1,j} = \sum_{m=1}^{3} \mathcal{W}_m.$$

Alternatively, we may also use the Roe solver for the solution of the Riemann problem; see Section 3.2.2. In this case, based on the solution of the linear problem (38) in the $x$-direction,

$$\partial_t q + \hat{A}\big(Q^n_{ij}, Q^n_{i-1,j}\big)\partial_x q = 0,$$

we obtain the propagating speeds, $\lambda_1 = \hat{u} - \hat{c}$, $\lambda_2 = \hat{u}$, $\lambda_3 = \hat{u} + \hat{c}$, and the jumps, $\mathcal{W}_1 = \hat{\alpha}_1\hat{r}_1$, $\mathcal{W}_2 = \hat{\alpha}_2\hat{r}_2 + \sum_{k=4}^{9}\hat{\alpha}_k\hat{r}_k$, $\mathcal{W}_3 = \hat{\alpha}_3\hat{r}_3$. Here the strengths across the discontinuties are of the form

$$\hat{\alpha}_2 = \Delta q^{(1)} + \frac{\hat{\Gamma}}{\hat{c}^2}\Big[-\frac{\hat{u}^2+\hat{v}^2}{2}\Delta q^{(1)} + \hat{u}\Delta q^{(2)} + \hat{v}\Delta q^{(3)} - \Delta q^{(4)} + \hat{p}\big(\Delta q^{(8)} - \Delta q^{(5)}\big) + \Delta q^{(6)} + \Delta q^{(7)}\Big],$$

$$\hat{\alpha}_3 = \frac{1}{2\hat{c}}\big[(\hat{c}-\hat{u})\Delta q^{(1)} + \Delta q^{(2)} - \hat{c}\hat{\alpha}_2\big], \quad \hat{\alpha}_1 = \Delta q^{(1)} - \hat{\alpha}_2 - \hat{\alpha}_3,$$

$$\hat{\alpha}_4 = \Delta q^{(4)} - \hat{v}(\Delta\rho - \hat{\alpha}_2), \qquad \hat{\alpha}_5 = \Delta q^{(5)} - \hat{\varphi}(\Delta\rho - \hat{\alpha}_2),$$

$$\hat{\alpha}_6 = \Delta q^{(6)} - \hat{\varphi}\hat{\mathcal{B}}(\Delta\rho - \hat{\alpha}_2), \qquad \hat{\alpha}_7 = \Delta q^{(7)} - \hat{\chi}(\Delta\rho - \hat{\alpha}_2),$$

$$\hat{\alpha}_8 = \Delta q^{(8)}, \qquad \hat{\alpha}_9 = \Delta q^{(9)},$$

with $\hat{v}$ computed by (28) and $\hat{c}^2 = \hat{\Gamma}[\hat{H} - (\hat{u}^2+\hat{v}^2)/2 + \hat{p}\hat{\varphi} - \hat{\varphi}\hat{\mathcal{B}} - \hat{\chi}]$. Note that the other averaged states appearing in the above formulae are set in the same manner as described in Section 3.2.2.

It is clear that no matter what shock-only or Roe solver is employed to the Riemann problem, if the wave speed $\lambda_l < 0$ the $l$th wave propagates into cell $(i-1, j)$, while if $\lambda_l > 0$ it propagates into cell $(i, j)$. In the simplest case of the wave propagation method, i.e., a two-dimensional extension of Godunov's method, the cell average affected by this wave is simply updated by $(\lambda_l \Delta t/\Delta x)\mathcal{W}_l$. Note that the quantity in parentheses is the fraction of the cell swept out by this wave; see Fig. 6a. By computing the effect of each wave to the cell averages, a single time step of the solution algorithm is completed.

It is well known that Godunov's method which we have just described has a very limited time step restriction for stability [36]. To improve upon the algorithm, by following an approach proposed by LeVeque [34], we introduce "transverse propagation" of these waves in the $x$-direction, so that they affect the cells above or below row $j$ as well, based on the propagation speeds in the $y$-direction. We do this for each wave individually in which with the shock-only solver we solve a Riemann problem for the equation

$$\partial_t q + g(\partial_y, q) = 0$$

and data $Q_L$ and $Q_R$ just to the left and right of the wave, while with the Roe solver we use the linear equation

$$\partial_t q + \hat{A}(Q_L, Q_R)\partial_y q = 0$$

instead. Considering the $l$th wave mentioned above, for example. This amounts to setting

$$Q_L = Q^n_{i-1,j} + \sum_{m=1}^{l-1} \mathcal{W}_m, \quad Q_R = Q_L + \mathcal{W}_l,$$

and leads to a splitting of the wave into three pieces,

$$\mathcal{W}_l = Q_R - Q_L = \sum_{m=1}^{3} \mathcal{W}_{lm},$$

where each subwave propagates at a speed $\mu_m$ in the $y$-direction, for $m = 1, 2, 3$. Figure 6b shows a typical example of the $\mu_m > 0$ case, where the wave $\mathcal{W}_{lm}$ is used to update the cell averages in cells $(i, j)$ and $(i, j+1)$, based on the area that the wave overlaps each cell,

$$Q^{n+1}_{ij} := Q^{n+1}_{ij} - \left(\lambda_l \frac{\Delta t}{\Delta x}\right)\left(1 - \frac{1}{2}\mu_m \frac{\Delta t}{\Delta y}\right)\mathcal{W}_{lm},$$

$$Q^{n+1}_{i,j+1} := Q^{n+1}_{i,j+1} - \frac{1}{2}\left(\lambda_l \frac{\Delta t}{\Delta x}\right)\left(\mu_m \frac{\Delta t}{\Delta y}\right)\mathcal{W}_{lm}.$$

Note that we have employed a standard initialization procedure that assigns each cell average to its values at the previous time step, $Q^{n+1}_{ij} = Q^n_{ij}$ for all $i, j$.

It should be mentioned that there exists an alternative transverse-propagation approach based on the splitting of numerical upwind or downwind fluxes instead (cf. [37, 39, 43]). This latter approach is often useful for a flux formulation of the wave-propagation schemes, whenever the equations to be solved can be written in a full conservation form, such as the single component of the Euler equations of gas dynamics. Here, because our model system (36) is written in a quasi-conservative form, it is not convenient to use that method as a basis for numerical approximation (cf. [60, 61] for a related work). In fact, we find it is robust to use the method in wave-propagation form such that we are able to handle each wave in turn and there is no need to compute fluxes and make distinction between the waves.

Undoubtedly, this modified version of Godunov's method belongs to a class of unsplit multidimensional upwind schemes. For a scalar problem, in particular, this approach is a variant of the corner transport upwind method of Colella [11] in that the cell averages at the

next time step can be interpreted as a linear combination of the neighboring cell values at the old time with suitable weights. To make this clear (see [38] also), we consider a linear advection equation

$$\partial_t q + u\partial_x q + v\partial_y q = 0,$$

with a positive particle velocity $(u, v) > 0, q \in \mathbb{R}$, as an example. Denote $\nu_x = u\Delta t/\Delta x$ and $\nu_y = v\Delta t/\Delta y$. The update of the cell average in terms of the jumps across each cell interface, say for the case of $Q_{ij}^n$ shown in Fig. 6b for example, can be found by

$$\begin{aligned} Q_{ij}^{n+1} = Q_{ij}^n - \nu_x\left(1 - \frac{1}{2}\nu_y\right)\left(Q_{ij}^n - Q_{i-1,j}^n\right) - \nu_y\left(1 - \frac{1}{2}\nu_x\right)\left(Q_{ij}^n - Q_{i,j-1}^n\right) \\ - \frac{1}{2}\nu_x\nu_y\left(Q_{i,j-1}^n - Q_{i-1,j-1}^n\right) - \frac{1}{2}\nu_x\nu_y\left(Q_{i-1,j}^n - Q_{i-1,j-1}^n\right). \end{aligned}$$

After a simple reorganization of terms, it can then be viewed as a sum of the transport of the neighboring states into the cell,

$$Q_{ij}^{n+1} = (1 - \nu_x - \nu_y)Q_{ij}^n + \nu_x(1 - \nu_y)Q_{i-1,j}^n + \nu_y(1 - \nu_x)Q_{i,j-1}^n + \nu_x\nu_y Q_{i-1,j-1}^n,$$

within a time step $\Delta t$ (cf. Fig. 1 of [11]). For convenience, we may write the above scheme to a more general form as

$$Q_{ij}^{n+1} = \sum_{l=0}^{1}\sum_{m=0}^{1} a_{lm} Q_{i-l,j-m}^n,$$

with the coefficients defined by $a_{00} = (1 - \nu_x - \nu_y)$, $a_{10} = \nu_x(1 - \nu_y)$, $a_{01} = \nu_y(1 - \nu_x)$, and $a_{11} = \nu_x\nu_y$. The method is clearly a monotone scheme and hence first-order accurate, as long as the time step $\Delta t$ satisfies the CFL condition $\max(\nu_x, \nu_y) \le 1$. It is not difficult to show that in the case of an interface only problem with uniform pressure and particle velocity, the pressure obtained using the method would remain in equilibrium without any spurious oscillations near the interfaces; see [65] for the details. Concerning stability of the full nonlinear system (36), it is observed numerically that the method is stable and convergent under mesh refinement provided that the waves in the method affect only the cells adjacent to the interface during the time step; see Section 4.3 for numerical examples.

*4.2.2. High resolution corrections.* To achieve high resolution, we begin by looking at the Taylor series expansion of the state vectors $q(x, y, t + \Delta t)$ at time $t$,

$$\begin{aligned} q(x, y, t + \Delta t) &= q(x, y, t) + \Delta t\partial_t q(x, y, t) + \frac{1}{2}(\Delta t)^2\partial_{tt} q(x, y, t) + \cdots \\ &= q(x, y, t) - \Delta t(A\partial_x q + B\partial_y q)(x, y, t) + \frac{1}{2}(\Delta t)^2\left[\partial_x\left(A^2\partial_x q\right)\right. \\ &\quad \left. + \partial_x(AB\partial_y q) + \partial_y(BA\partial_x q) + \partial_y\left(B^2\partial_y q\right)\right](x, y, t) + \cdots, \end{aligned}$$

where with the aid of (38) we have replaced the time derivatives $\partial_t q$ and $\partial_{tt} q$ by the respective spatial derivatives. Clearly, from the basic local truncation error analysis, to

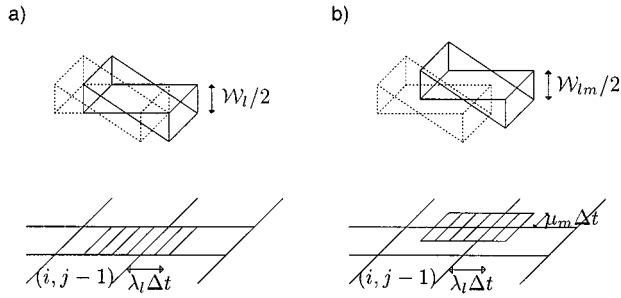


**FIG. 7.** High-resolution wave propagation methods. (a) Normal propagation of the correction wave, a case with $\lambda_l > 0$ is shown. (b) Transverse propagation of correction wave, a case with the splitting of the $l$th wave shown in (a). Only the $m$th subwave is plotted, $\mu_m > 0$. The piecewise-linear wave form in dashed lines is the initial location of the correction wave before propagation. The cell averages affected by the correction wave are updated by the volume of the interaction between the wave and grid cell.

achieve second-order accuracy of the method, we need to include an approximation to the $O(\Delta t^2)$ term:

$$\partial_{tt} q = \partial_x \left(A^2 \partial_x q\right) + \partial_x (AB \partial_y q) + \partial_y (BA \partial_x q) + \partial_y \left(B^2 \partial_y q\right).$$

In pursuit of implementing this efficiently, it turns out that the transverse-wave splitting method described in Section 4.2.1 has already given a way to approximate the terms: $\partial_x (AB \partial_y q)$ and $\partial_y (BA \partial_x q)$ (cf. [37]). Thus, to achieve full second-order accuracy, we need only add in the $\partial_x (A^2 \partial_x q)$ and $\partial_y (B^2 \partial_y q)$ terms to the method. By following the one-dimensional case, one standard procedure is to first introduce correction waves in a piecewise-linear form, propagate the wave normal to the interface over the time step $\Delta t$, and then update the cell averages it overlaps.

Consider the $l$th wave shown in Fig. 7a, for example. The corrections are accomplished by the updates

$$Q_{ij}^{n+1} := Q_{ij}^{n+1} + \frac{1}{2}\left(|\lambda_l| \frac{\Delta t}{\Delta x}\right)\left(1 - |\lambda_l| \frac{\Delta t}{\Delta x}\right)\mathcal{W}_l,$$
$$Q_{i-1,j}^{n+1} := Q_{i-1,j}^{n+1} - \frac{1}{2}\left(|\lambda_l| \frac{\Delta t}{\Delta x}\right)\left(1 - |\lambda_l| \frac{\Delta t}{\Delta x}\right)\mathcal{W}_l,$$

where the factors multiplying $\mathcal{W}_l$ are simply the fractions of each cell that are overlapped by the correction wave. In practice, the strength of each wave is limited using a "slope-limiter" [70], and so each $\mathcal{W}_l$ in the above correction is replaced by a limited value $\widetilde{\mathcal{W}}_l$; see Section 3.3.2 for the details.

It should be noted that we may improve upon the method further (although it is still second-order accurate) by introducing transverse propagation of correction waves as well. In this instance, the $\mathcal{W}_{lm}$ (see Section 4.2.1) is used to update cell averages wherever it is affected; see Fig. 7b. The updates are

$$Q_{ij}^{n+1} := Q_{ij}^{n+1} + \frac{1}{2}\left(|\lambda_l| \frac{\Delta t}{\Delta x}\right)\left(1 - |\lambda_l| \frac{\Delta t}{\Delta x}\right)\left(1 - |\mu_m| \frac{\Delta t}{\Delta y}\right)\mathcal{W}_{lm},$$
$$Q_{i-1,j}^{n+1} := Q_{i-1,j}^{n+1} - \frac{1}{2}\left(|\lambda_l| \frac{\Delta t}{\Delta x}\right)\left(1 - |\lambda_l| \frac{\Delta t}{\Delta x}\right)\left(1 - |\mu_m| \frac{\Delta t}{\Delta y}\right)\mathcal{W}_{lm},$$

$$Q^{n+1}_{i,j+1} := Q^{n+1}_{i,j+1} + \frac{1}{2}\left(|\lambda_l|\frac{\Delta t}{\Delta x}\right)\left(1 - |\lambda_l|\frac{\Delta t}{\Delta x}\right)\left(|\mu_m|\frac{\Delta t}{\Delta y}\right)\mathcal{W}_{lm},$$

$$Q^{n+1}_{i-1,j+1} := Q^{n+1}_{i-1,j+1} - \frac{1}{2}\left(|\lambda_l|\frac{\Delta t}{\Delta x}\right)\left(1 - |\lambda_l|\frac{\Delta t}{\Delta x}\right)\left(|\mu_m|\frac{\Delta t}{\Delta x}\right)\mathcal{W}_{lm}.$$

It can be shown that when handling all the correction waves in this way, we have a consistent approximation to the third order terms $BA^2\partial_{xxy}q$ and $AB^2\partial_{yyx}q$; see [38] for a detailed analysis to a scalar problem. Based on various numerical evidences, we find that this modified method with transverse propagation of correction waves works slightly better than that with normal propagation of the waves (judging from how the symmetry of the solution structure is preserved, for example). Hence, the high-resolution results present in Section 4.3 use exclusively the transverse-propagation version of the method for experiments.

### 4.3. *Numerical Results*

We now present some sample results obtained using our multicomponent algorithm with the Roe solver described in Section 4.2. It is our purpose to demonstrate the effectiveness of our algorithm for a reasonable class of problems of practical importance.

EXAMPLE 4.3.1. We begin by considering an interface only problem where the solution consists of a circular gas bubble evolving in a liquid with uniform equilibrium pressure $p_0 = 10^5$ Pa and constant particle velocity $(u_0, v_0) = (10^3$ m/s, $10^3$ m/s). Inside the bubble of radius $r_0 = 0.16$ m, the fluid is a van der Waals gas with

$$(\rho, \gamma, a, b)_{r\le r_0} = (50 \text{ kg/m}^3, 1.4, 5 \text{ Pa m}^6/\text{kg}, 10^{-3} \text{ m}^3/\text{kg}),$$

while outside the bubble, the fluid is a liquid modeled by a stiffened gas with

$$(\rho, \gamma, \mathcal{B})_{r>r_0} = (10^3 \text{ kg/m}^3, 4.4, 6 \times 10^8 \text{ Pa}).$$

Here $r = \sqrt{(x - x_0)^2 + (y - y_0)^2}$ is the distance from a point $(x, y)$ in a unit square domain to the center of the bubble $(x_0, y_0) = (1/4$ m, $1/4$ m).

Results obtained using the high-resolution version of the method with a $100 \times 100$ grid are shown in Fig. 8, where the 2D contours of the density, 3D surface plot of pressure, and the cross-section plot of the density and pressure along $x = y$ are presented at time $t = 360\ \mu$s. From the displayed profiles, it is easy to observe good agreement of the numerical solutions as compared with the exact results. Notice that the computed pressure remains in the correct equilibrium state $p_0$ (to be more accurate, the difference of these two is only on the order of machine epsilon), without any spurious oscillations near the bubble interface. Moreover, the bubble retains its circular shape and appears to be very well located also.

EXAMPLE 4.3.2. We are next concerned with a radially symmetric problem such that the computed solution in two dimensions can be compared to the one-dimensional results for numerical validation. We use the following set of two-phase (liquid–gas) flow data for experiments in which, in the gas phase, the state variables are

$$(\rho, p, \gamma, a, b)_{r\le r_0} = (1250 \text{ kg/m}^3, 10^9 \text{ Pa}, 1.4, 1 \text{ Pa m}^6/\text{kg}, 10^{-4} \text{ m}^3/\text{kg}),$$

while in the liquid phase they are

$$(\rho, p, \gamma, \mathcal{B})_{r>r_0} = (10^3 \text{ kg/m}^3, 10^5 \text{ Pa}, 4.4, 6 \times 10^8 \text{ Pa}),$$

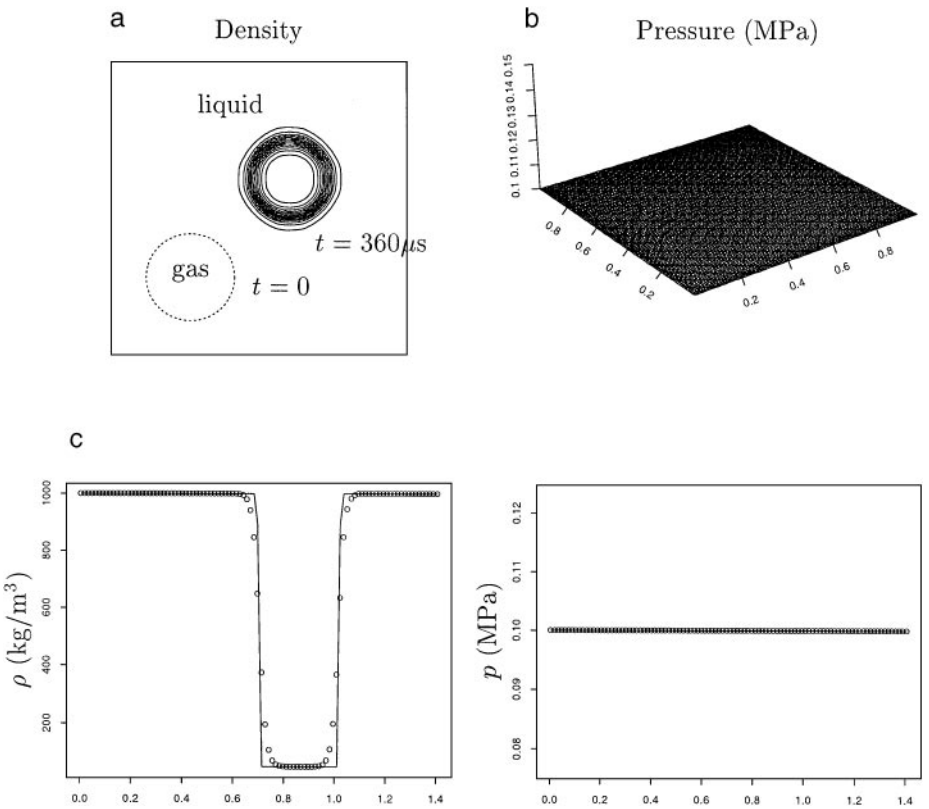


**FIG. 8.** High-resolution results for an interface-evolving problem at time $t = 360$ $\mu$s. (a) Contour plot of the density. (b) Surface plot of the pressure. (c) Cross-sectional plots of density and pressure along line $x = y$. The solid line in the cross-sectional plot is the exact solution, and the dotted points are the numerical results. The dashed line in the density contour plot is the initial location of the gas bubble at time $t = 0$.

where $r^2 = x^2 + y^2$ and $r_0 = 1/5$ m. Initially both the gas and liquid are in a stationary position, but due to the pressure difference between the fluids, breaking of the circular membrane at $r_0$ occurs instantaneously. For this problem, the resulting solution consists of an outward-going shock wave in liquid, an inward-going rarefaction wave in gas, and a contact discontinuity lying in between that separates the gas and the liquid. We note that because of the geometric symmetry of the solution, for simplicity, we only take a quarter of the unit square domain, i.e., $(x, y) \in ([0, 1/2] \times [0, 1/2])$ m$^2$, and apply the line of symmetry boundary conditions to the bottom and the left boundaries during the computation.

In Fig. 9, we show numerical results for the density, radial velocity (defined as $\bar{u} = \sqrt{u^2 + v^2}$), and pressure at time $t = 120$ $\mu$s, where the test has been carried out by using a $200 \times 200$ grid with the high-resolution method. Clearly, from Fig. 9a, we observe good resolution of the wave pattern (i.e., both the shock and interface remain circular and appear to be very well located) after the breaking of the membrane. Note that there are little wiggles on the contours of $\bar{u}$ near the $x$- and $y$-axis which signifies grid-alignment effects with the use of the Roe solver (cf. [42] for a similar problem in astrophysics). It should be mentioned that this type of error is already present when the problem is solved by using the first order method (not shown). However, we obtain a better result while performing the test as in Fig. 9 with the shock-only Riemann solver; see Fig. 10. Here the dashed line shown in the figure is the approximate location of the interface.

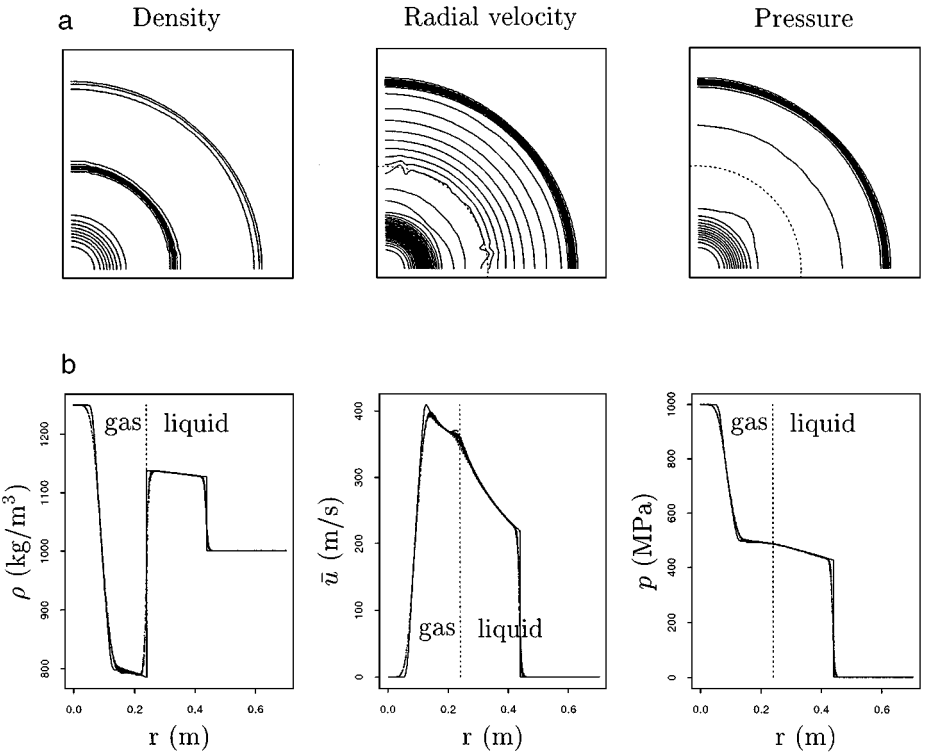


**FIG. 9.** High-resolution results for a radially symmetric problem at time $t = 120$ $\mu$s. (a) Contours of the density, radial velocity, and pressure. (b) Scatter plots of $\rho$, $\bar{u}$, and $p$ with locations measured at a distance from the cell center to the origin. The solid line in the scatter plot is the "true" solution obtained from solving the one-dimensional model with appropriate source terms for the radial symmetry using the high-resolution method. The dotted points are the two-dimensional result. The dashed line shown in the figure is the approximate location of the interface.

The scatter plots shown in Fig. 9b provide the validation of our two-dimensional results as in comparison with the "true" solution obtained from solving the one-dimensional model with appropriate source terms for the radial symmetry, using the high-resolution method with a 1000 mesh points. That is, for the equation, we have a modified version of the one-dimensional model (13) as

$$\partial_t q + f(\partial_r, q) = \psi(q) \tag{40}$$

with $f$ a vector-value function defined by

$$f = \Bigg[\partial_r(\rho u),\, \partial_r(\rho u^2 + p),\, \partial_r(\rho E u + p u),\, \partial_r\left(\frac{b\rho}{\gamma - 1}u\right),$$
$$\partial_r\left(\frac{\gamma - b\rho}{\gamma - 1}\mathcal{B}\right) - \left(\frac{\gamma\mathcal{B}}{\gamma - 1}\right)\partial_r u,\, \partial_r\left(\frac{2 - \gamma - b\rho}{\gamma - 1}a\rho^2 u\right) + \left(\frac{2 - \gamma - 2b\rho}{\gamma - 1}a\rho^2\right)\partial_r u,$$
$$u\partial_r\left(\frac{1}{\gamma - 1}\right),\, u\partial_x a\Bigg]^T$$

and $\psi$ the source term derived directly from the geometric simplification of a

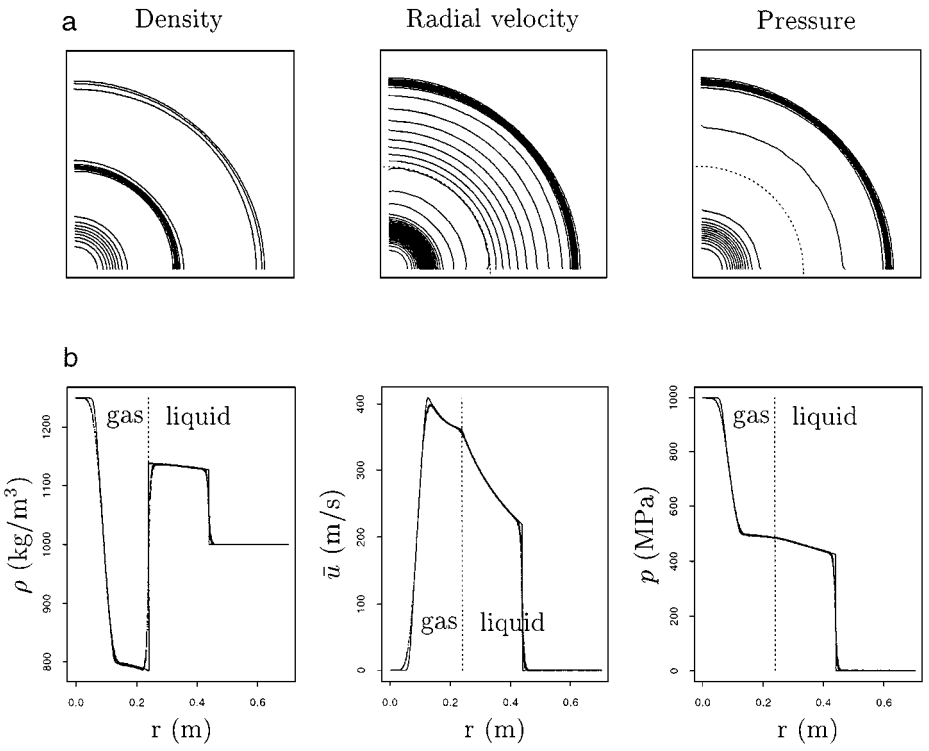


**FIG. 10.** Results for the same run as performed in Fig. 9 but obtained by using the shock-only Riemann solver to the method.

multidimensional flow to a one-dimensional one,

$$\psi = -\frac{\kappa}{r}\left[\rho u, \rho u^2, \rho E u + pu, \frac{b\rho}{\gamma - 1}u, \frac{-b\rho}{\gamma - 1}\mathcal{B}u, \frac{4 - 2\gamma - 3b\rho}{\gamma - 1}a\rho^2 u, 0, 0\right]^T.$$

Note that here the source term is constructed in such a way that (40) reduces to a typical quasi-one-dimensional model for single-component flows [45], when there is no jump on each of the material-dependent quantities $\gamma, a, b$, and $\mathcal{B}$ across the interfaces. In the case of a 2D radially or 3D spherically symmetric flow, we have the quantity $\kappa = 1$ or 2, respectively; $u$ now denotes the particle velocity in the $r$- (radial) direction. We use a Strang-type time splitting procedure to deal with the geometric sources of (40) in a high-resolution manner[67].

A more detailed study of the solutions under mesh refinement may be found in [65] for a simpler case with the Tait equation of state for the liquid and the constant covolume equation of state for the gas. In that reference, extensions of our two-dimensional model to cases with geometric and gravitational sources are briefly discussed also.

EXAMPLE 4.3.3. To show how our algorithm works on shock waves, we consider the simulation of a shock wave in liquid over a gas bubble. The aim of the test performed here is twofold: the first is to further validate convergence of the computed solutions obtained using our multicomponent algorithm to the correct weak ones, and the second is to provide an example that shows the feasibility of the algorithm as applied to practical problems. We note that this problem is of practical importance to many applications in sciences and engineering (see [6, 8, 16] and references therein for more information).

To set up the test, we take a vertical shock tube of size $[0, 1] \times [-0.2, 1]$ m$^2$ and consider a planarly downward-moving Mach 1.422 shock wave in liquid with data in the preshock

state as

$$(\rho, u, v, p)^{(l)}_{\text{preshock}} = (10^3 \text{ kg/m}^3, 0, 0, 10^5 \text{ Pa}),$$

and data in the postshock state as

$$(\rho, u, v, p)^{(l)}_{\text{post-shock}} = (1.23 \times 10^3 \text{ kg/m}^3, 0, -432.69 \text{ m/s}, 10^9 \text{ Pa}).$$

The equation of state parameters we employed for the liquid are the same as before; namely, $\gamma = 4.4$ and $\mathcal{B} = 6 \times 10^8$ Pa. In addition to the shock wave, we assume there is a stationary gas bubble of radius $r_0 = 1/5$ m located at $(x_0, y_0) = (1/2 \text{ m}, 1/2 \text{ m})$ just below the shock and that is about to interact with the shock; see Fig. 11 for an illustration. Inside the gas

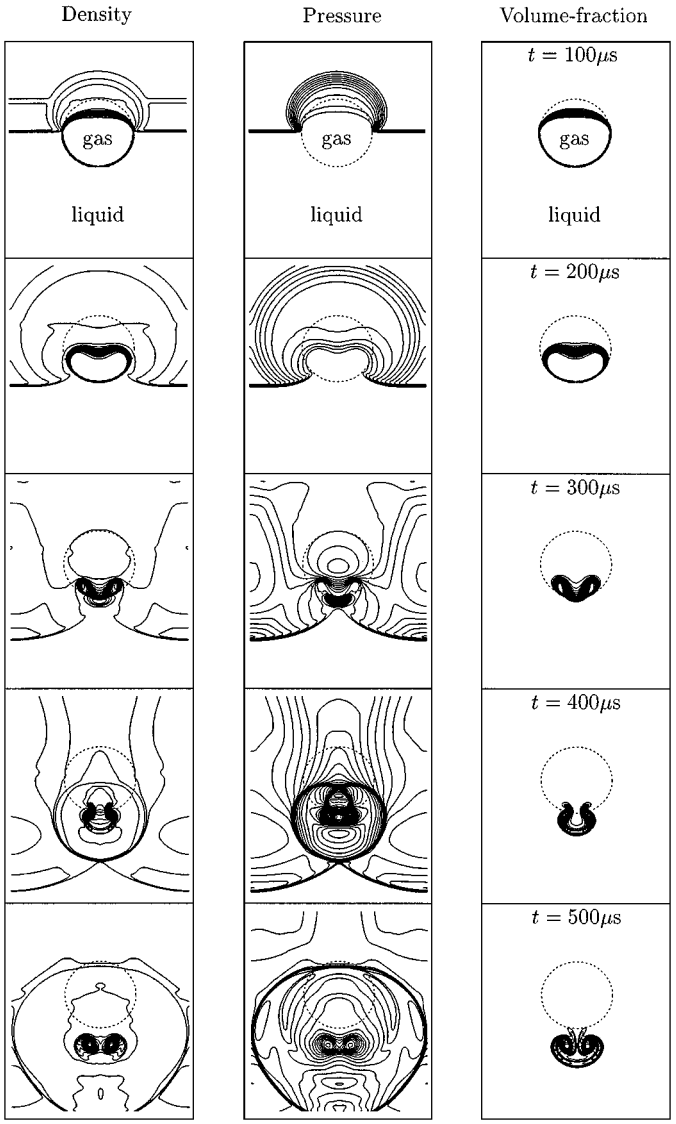


**FIG. 11.** High-resolution results for a planar Mach 1.422 shock wave in liquid over a gas bubble. Contours of $\rho$, $p$, and $Y$ (volume fraction of the gas) are shown at five different times; $t = (1, 2, 3, 4, 5) \cdot 10^2$ $\mu$s. The circular dashed line appearing in the plots is the initial location of the interface.

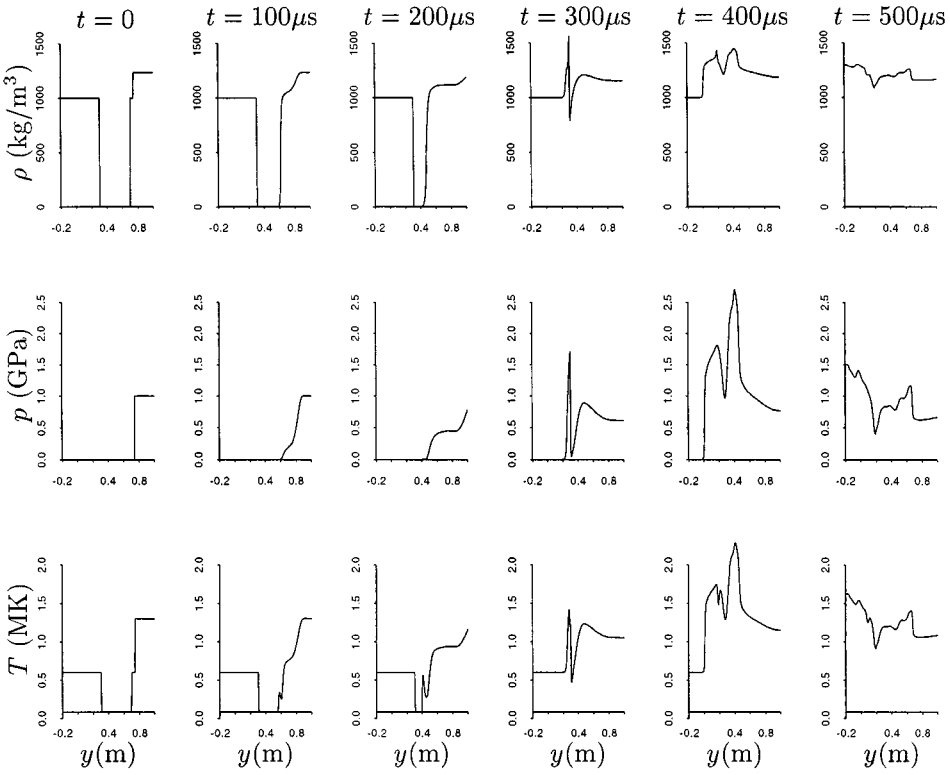


**FIG. 12.** Cross-sectional plots of the results for the run shown in Fig. 11 along $x = 1/2$ m.

bubble, the state variables are assigned by

$$(\rho,\, p,\, \gamma,\, a,\, b)^{(\mathrm{g})} = (1.2\ \mathrm{kg/m^3},\, 10^5\ \mathrm{Pa},\, 1.4,\, 10^{-3}\ \mathrm{m^3/kg},\, 5\ \mathrm{Pa\ m^6/kg}).$$

Note that because of the large pressure jump across the shock wave and also the large ratio of the acoustic impedances of the liquid to gas, $(\rho c)^{(\ell)}/(\rho c)^{(\mathrm{g})} \approx 3965$, this is a harder problem to solve in practice.

Figures 11 and 12 show high-resolution results of a sample run using a $200 \times 240$ grid. From Fig. 11, reasonable resolutions of the solution structure (i.e., the distortion of the gas bubble and the somewhat complicated wave patterns after the passage of the shock to the bubble) are obtained by using the algorithm where contours of $\rho$, $p$, and $Y$ (volume fraction of the gas, introduced in the computation for monitoring the evolution of the gas bubble) are presented at five different times, $t = (1, 2, 3, 4, 5) \cdot 10^2$ $\mu$s; see [17, 25, 57, 60] for a similar test of the problem. The cross-section of the results for the same run along line $x = 1/2$ m is drawn in Fig. 12, giving some quantitative information about the density, pressure, and temperature at the selected times.

To check the correctness of the computed solutions, Fig. 13 shows results of a convergence study of $\rho$, $p$, and $T$ along line $x = 1/2$ m, at the final stopping time $t = 500$ $\mu$s. Noting the sensible convergence behavior of the solution profiles under mesh refinement, where we have used a grid sequence, $2^i(100 \times 120)$ for $i = 0, 1, 2$, for the test. See [65] for a preliminary result of the problem over an array of gas bubbles.

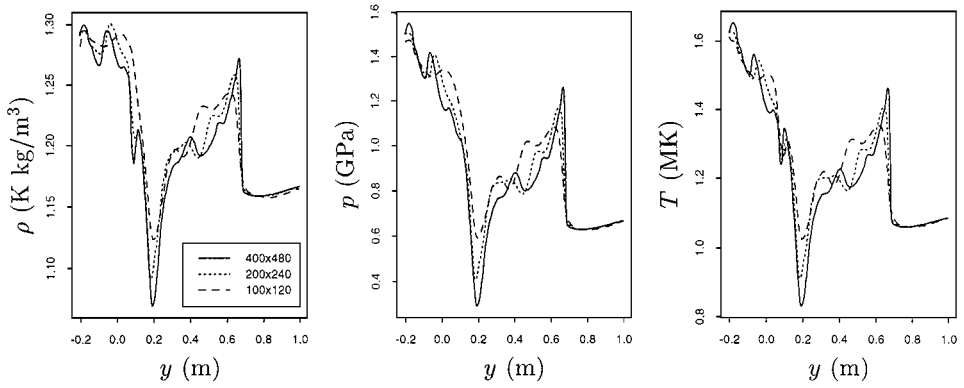


**FIG. 13.** A convergence study of $\rho$, $p$, and $T$ for a planar Mach 1.422 shock wave in liquid over a gas bubble. The test is performed by using a high-resolution version of the method with three different grid systems: $2^i \cdot (100 \times 120)$, $i = 0, 1, 2$. Only the cross-sectional solutions along $x = 1/2$ m at time $t = 500$ $\mu$s are presented.

## 5. SLIP LINE PROBLEMS AND CORRECTIONS

Motivated by the work of Saurel and Abgrall [60] on slip lines (i.e., a contact discontinuity with jumps on the tangential velocities) for multicomponent problems, we now examine how our two-dimensional algorithm works for such a class of problems.

### 5.1. *Preliminary*

We begin by considering a simple numerical test in which the solution is a plan interface moving vertically by $u_0 = 10^3$ m/s in the $x$-direction that separates the tangential velocities $v_L = -5 \times 10^3$ m/s on the left and $v_R = 10^3$ m/s on the right of the interface. For convenience, we use the same two-phase flow setup as in Example 3.4.1 where the pressure is uniform with $p_0 = 10^5$ Pa in a two-dimensional shock tube of size $[0, 1] \times [0, 1/10]$ m$^2$ and the fluid is a gas and liquid on the left and right of the interface, respectively. Note that this is a different kind of interface only problem that exists only in multiple space dimensions.

For this problem, we do the test using the first order wave propagation method with the Roe solver as usual; see Section 4.2. Results of a sample run with a $200 \times 20$ grid are shown in Fig. 14 at time $t = 360$ $\mu$s. From the figure, large errors in both the pressure and particle velocity in the $x$-direction are clearly seen. Carrying out more tests to the problem, we find that these errors remain at about the same order of magnitude as the mesh is refined and become even erroneous when a high-resolution method is employed instead. We note that this observation of the error is true also when we solve the problem using the shock-only Riemann solver. In fact, by following a similar analysis to that conducted in [60], we may explain the observed error behavior as being the failure to approximate the kinetic energy in the tangential direction, $\mathcal{K}^{(t)} = \rho v^2/2$, consistently by the method. Because of this, the pressure computed via (37) would not yield the accurate result that is in equilibrium with $p_0 = 10^5$ Pa. Note that this is a difficult problem to solve in practice and is even so in the single component case of the problem; see [80] for a general remark on numerical errors which occurred in this class of problem with Godunov-type schemes.

For this model slip line problem, analogously to the work done in [60], it is easy to improve upon the result by solving an extended one-dimensional system that combines the $x$-sweep of our two-dimensional model, $\partial_t q + f(\partial_x, q) = 0$, see (36), with an additional

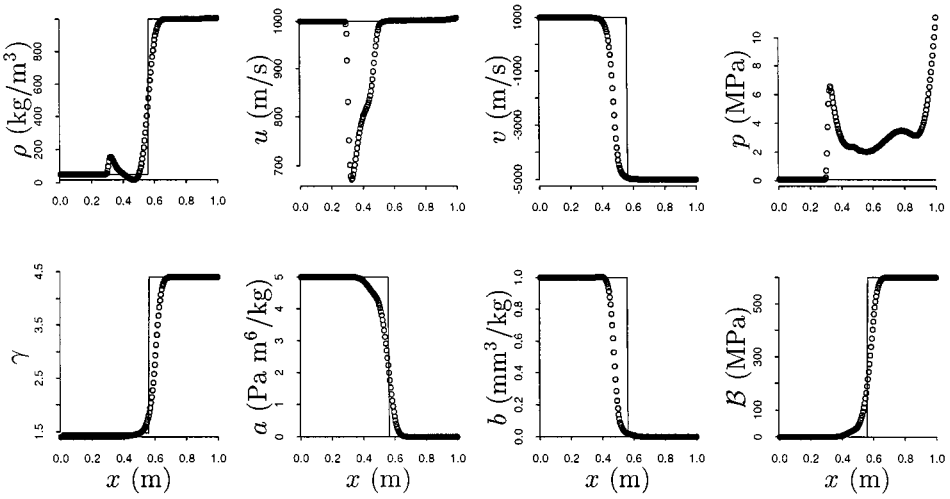


**FIG. 14.** Preliminary results for a model slip line problem at time $t = 360\ \mu$s; the first order method with the multicomponent model (36). The solid line is the exact solution and the points show the computed solution with a $200 \times 20$ grid; only the solution along the cross-section of $y = 1/20$ m is presented.

transport equation for the tangential kinetic energy $\mathcal{K}^{(t)}$,

$$\partial_t \mathcal{K}^{(t)} + \partial_x \left( \mathcal{K}^{(t)} u \right) = 0. \tag{41}$$

Note that we have taken the above equation to be of the form that works even for shock and rarefaction waves as well. Rather than computing the pressure based on (37), which incurs large errors as shown in Fig. 14, here we use the following modified version,

$$p = \left[ \rho E - \frac{(\rho u)^2}{2\rho} - \mathcal{K}^{(t)} - \left( \frac{\gamma - b\rho}{\gamma - 1} \mathcal{B} \right) - \left( \frac{2 - \gamma - b\rho}{\gamma - 1} a\rho^2 \right) \right] \Big/ \left( \frac{1 - b\rho}{\gamma - 1} \right), \tag{42}$$

with $\mathcal{K}^{(t)}$ set by the solution of (41). Note that in the current slip line problem it is not difficult to show the inconsistency of the numerical solution $\mathcal{K}^{(t)} \neq (\rho v)^2/(2\rho)$. Numerical results present in Fig. 15 indicate that with the correction of $\mathcal{K}^{(t)}$ to (42) this is a good approach without introducing any artificial oscillations in $p$ and $u$, when performing the same test as in Fig. 14 with both the first order and high-resolution wave propagation methods. Observing the displayed profiles, the other components of the solutions are well behaved also.

It should be noted that no propagation of transverse waves and the solutions of the system in the $y$-direction, $\partial_t q + g(\partial_y, q) = 0$, have been included in the above computation. This is eligible to do for this problem which is one-dimensional in nature. The Roe solver of this extended system can be derived quite easily as in Sections 3.2.2 and 4.2 and has been used to produce the results present in Fig. 15.

To further test the above corrected algorithm with the improvement of $\mathcal{K}^{(t)}$ in the $x$-direction, we are next concerned with a two-phase liquid–gas Riemann problem studied by Saurel and Abgrall [60] in which the solution is composed of a leftward going rarefaction wave, a rightward going slip line, and a (weak) shock wave in front of the slip line. In this problem, we take the same initial data as concerned previously in Example 3.4.2, but

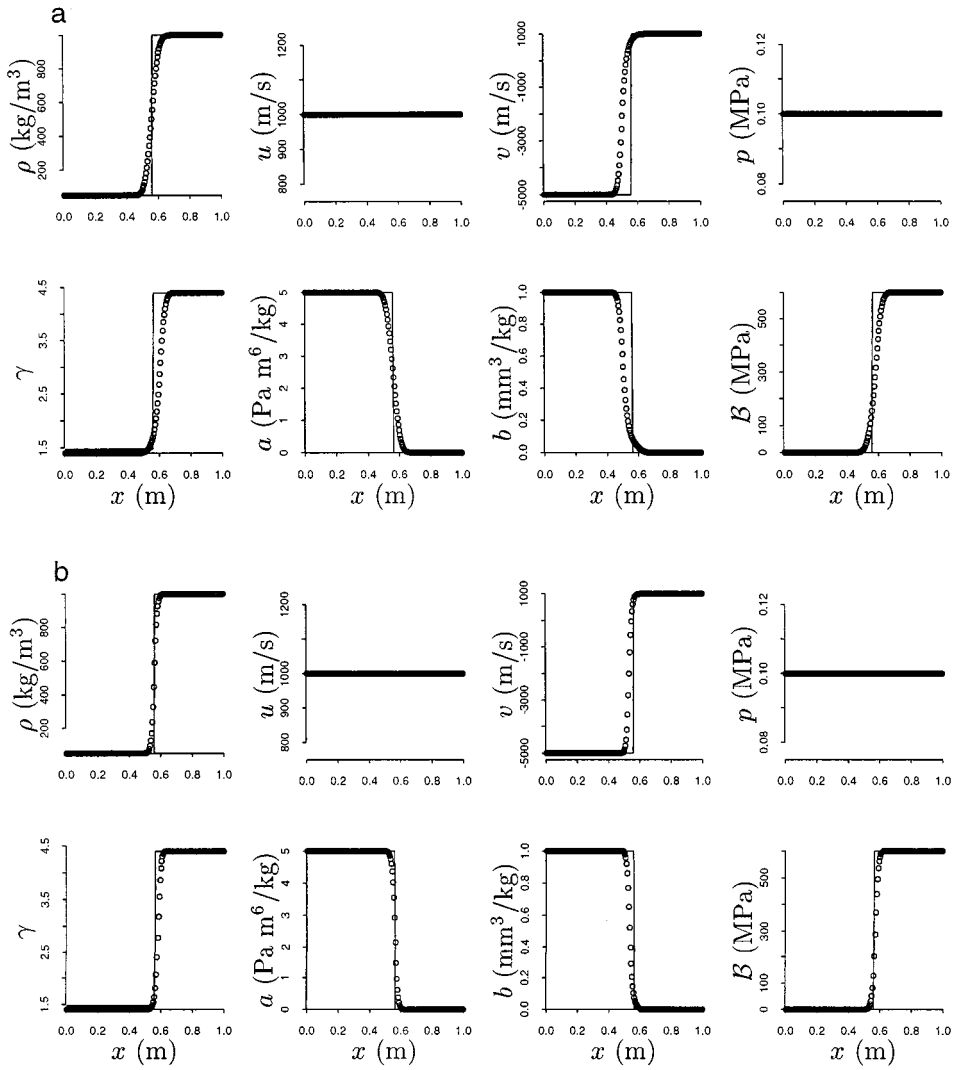


**FIG. 15.** Improved results of the test performed in Fig. 14; methods with the $x$-sweep of our two-dimensional model, $\partial_t q + f(\partial_x, q) = 0$, and the additional equation for the tangential kinetic energy (41). Results using (a) the first order wave propagation method and (b) the high-resolution wave propagation method. The Roe solver is employed to the computations.

impose additionally tangential velocities $v_L = 10^3$ m/s on the left and $v_R = -5 \times 10^3$ m/s on the right of the interface. The computational domain is again a two-dimensional shock tube of size $[0, 1] \times [0, 1/10]$ m$^2$. Surely, the region in the $y$-direction is also redundant for this problem.

Figure 16 shows results for a run obtained using the high-resolution method with a $200 \times 20$ grid up to time $t = 240$ $\mu$s, where the cross-section plots of $\rho$, $u$, $v$, and $p$ along $y = 1/20$ m are presented at the final stopping time. From the displayed graphs, despite the slight overshoot in $\rho$ and undershoot in $p$ at the tail of the rarefaction wave, see Fig. 4 also, we clearly observe the correct behavior of the computed slip line and also the rarefaction and shock waves as in comparison with the exact solution. We note that without using (42),

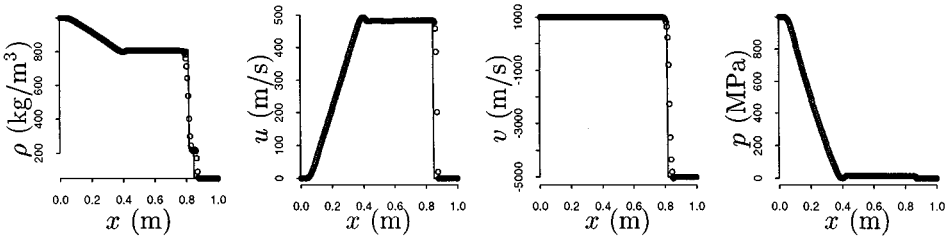


**FIG. 16.** High-resolution results for the Saurel–Abgrall liquid–gas Riemann problem at time $t = 240\ \mu$s. The solid line is the exact solution and the points show the computed solution with a $200 \times 20$ grid; only the solution along the cross-section of $y = 1/20$ m is presented.

the computed pressure obtained from (37) would become negative (which is nonphysical in the current case) within the first few time steps of the program execution. See [60] for the results of a similar calculation, where a MUSCL-type scheme is employed to solve the problem with the zero van der Waals gas constants: $a = 0$ and $b = 0$.

### 5.2. *An Improved Multidimensional Algorithm*

More generally, to be able to deal with multidimensional slip lines, shocks, and rarefaction waves at the same time, we should use the full set of the model system (36) and include suitable equations or schemes for the computation of the tangential kinetic energies in the $x$- and $y$-directions, respectively, yielding the accurate value for the pressure (cf. [60]). Since the numerical method we have described in Section 4.2 is an unsplit one, after various unsuccessful attempts to generalize the approach proposed in Section 5.1, it turns out to be most convenient to implement the method based on the shock-only Riemann solver with an additional update to the total kinetic energy $\mathcal{K} = \rho(u^2 + v^2)/2$ from the jumps of the Riemann problem solution across the waves. Note that like the update of the state variables $Q_{ij}^n$ to the solutions of (36), in our wave propagation method, there is no problem to compute the new value of $\mathcal{K}_{ij}^n$ independently over a time step $\Delta t$ by the scheme. In fact, it is not difficult to show that the method reduces essentially to the scheme proposed in Section 5.1 for one-dimensional slip line problems, when the shock-only Riemann solver is employed there. When the update step of both $Q_{ij}^n$ and $\mathcal{K}_{ij}^n$ is done, we may compute the pressure from the further revised formula of (42),

$$p_{ij}^{n+1} = \left[\rho E - \mathcal{K} - \left(\frac{\gamma - b\rho}{\gamma - 1}\mathcal{B}\right) - \left(\frac{2 - \gamma - b\rho}{\gamma - 1} a\rho^2\right)\right]_{ij}^{n+1} \Bigg/ \left(\frac{1 - b\rho}{\gamma - 1}\right)_{ij}^{n+1}, \quad (43)$$

that is typically more accurate than simply employing (36) and (37) to the slip line problems (see comments and results shown below). Of course, in case there is not any strong shear flow moving along the interface, such as for a radially symmetric flow considered in Section 4.3, numerical results obtained using these two different approaches would be quite similar, where the solution of $\mathcal{K}$ by the improved algorithm is approximately equal to $[(\rho u)^2 + (\rho v)^2]/(2\rho)$ obtained from using the solutions of the basic conservation laws.

It should be mentioned that because the transfer of the energy between the kinetic and potential energies is governed implicitly by the conservation law of the total energy, in the general multidimensional case, we thus do not have a model equation for the motion of the total kinetic energy explicitly. For this reason, it is not clear at all how to form a linear system

of the governing equations and use the Roe solver as a basis to the current formulation of the scheme. Notably, this is a problem that we will work on in the future to develop an unsplit multicomponent algorithm for slip lines with a simpler approximate Riemann solver; this may not be an easy task, however. Two sample calculations are performed below to show the usefulness of the improved algorithm for slip line problems.

EXAMPLE 5.2.1. As a first example, we consider a two-dimensional Reimann problem in which the initial condition is composed of four slip lines with the data in the four quadrants given by

$$(\rho, u, v, p)_1 = (\rho_0, u_0, -v_0, p_0), \quad (\rho, u, v, p)_2 = (2\rho_0, u_0, v_0, p_0),$$
$$(\rho, u, v, p)_3 = (\rho_0, -u_0, v_0, p_0), \quad (\rho, u, v, p)_4 = (3\rho_0, -u_0, -v_0, p_0),$$

where $\rho_0 = 10^3$ kg/m$^3$, $u_0 = 10^3$ m/s, $v_0 = 7 \times 10^2$ m/s, and $p_0 = 1$ GPa. In this problem, the fluid in the first and third quadrants is a gas with $\gamma = 1.4$, $a = 1$ Pa m$^6$/kg, and $b = 10^{-4}$ m$^3$/kg, while the fluid in the second and fourth quadrants is a liquid with $\gamma = 4.4$ and $\mathcal{B} = 6 \times 10^8$ Pa; the domain is a unit square. We note that this problem is a multicomponent version of a case studied by Schulz-Rinne *et al.* where after breaking the membranes the slip lines spiral around its center in a clockwise manner forming an interesting vortex-like structure (Fig. 9 of [62]).

In Fig. 17, we present high-resolution results obtained using a $200 \times 200$ grid and the improved method with the update of the total kinetic energy at time $t = 150$ $\mu$s. From the contours of the displayed quantities such as the density, particle velocities in the $x$- and $y$-direction, and pressure, we observe the very nice spiral structure of the computed solutions, without any artificial fluctuations near the slip lines. The cross-sectional plots of $\rho, u, v$, and $p$ for the same run along the line $x = 1 - y$ are shown in Fig. 18 where the solid line is the fine grid solution with a $400 \times 400$ grid. We see good agreement between the two solutions.

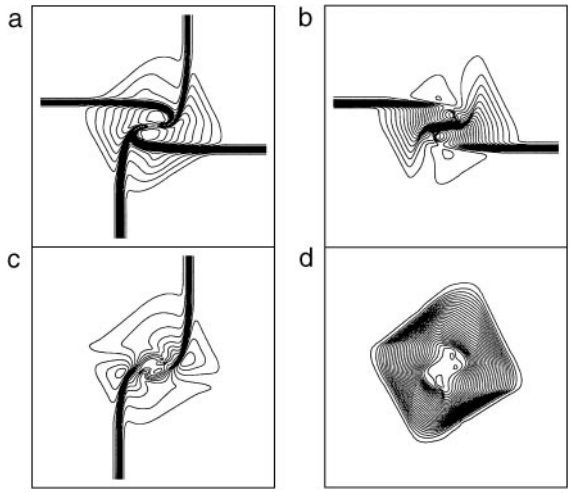


**FIG. 17.** High resolution results for a two-dimensional Riemann problem, a slip-lines only case. The result is obtained using a $200 \times 200$ grid and the improved method with the update of the total kinetic energy. Contours of the solutions for (a) density, (b) particle velocity in the $x$-direction, (c) particle velocity in the $y$-direction, and (d) pressure are shown at time $t = 150$ $\mu$s.

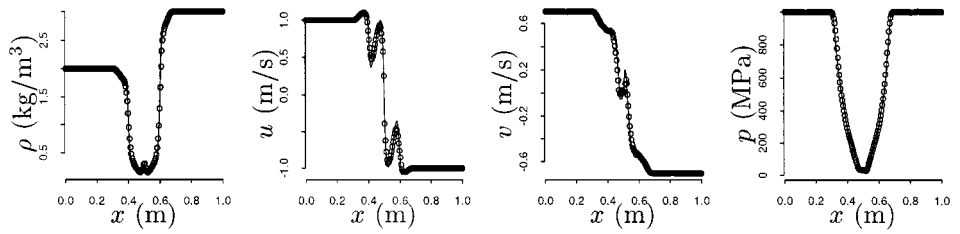


**FIG. 18.** Cross-sectional plots of $\rho$, $u$, $v$, and $p$ for the same run shown in Fig. 17 along $x = 1 - y$. The solid line is the fine grid solution with a $400 \times 400$ grid.

EXAMPLE 5.2.2. Our second example is again a two-dimensional Riemann problem, but with a different set of data where the state in the first quadrant is connected to the second and fourth quadrants by a 1-shock moving leftward and downward of the $x$- and $y$-directions, respectively. The state in the third quadrant is connect to the second and fourth quadrants by a slip line, however. This problem is a variant of a run considered in Fig. 12 of [62] where the interaction at the corner leads to a simple Mach reflection similar to what is seen in various shock reflections from boundaries. The data we use for the test are given by

$$(\rho, u, v, p)_1 = (\bar{\rho}, \bar{u}, \bar{u}, 3p_0), \qquad (\rho, u, v, p)_2 = (\rho_0, u_0, \bar{u}, p_0),$$
$$(\rho, u, v, p)_3 = (0.8\rho_0, \bar{u}, \bar{u}, p_0), \quad (\rho, u, v, p)_4 = (\rho_0, \bar{u}, v_0, p_0),$$

where $\rho_0 = 1$ kg/m$^3$, $u_0 = v_0 = 0$, $p_0 = 10^5$ Pa, and $\bar{\rho} = 2.1$ kg/m$^3$, $\bar{u} = 324.28$ m/s for a Mach 1.65 shock wave. In this problem, with the exception that the fluid in the third quadrant is a polytropic gas with $\gamma = 1.67$, the fluid in the other quadrants is a constant covolume gas with $\gamma = 1.4$ and $b = 10^{-3}$ m$^3$/kg.

We perform a similar test as in Example 5.2.1 using the improved high-resolution method, but with a finer $400 \times 400$ grid for checking convergence of the solutions. Results of a sample calculation at time $t = 800$ $\mu$s are shown in Figs. 19 and 20. From the contours of the

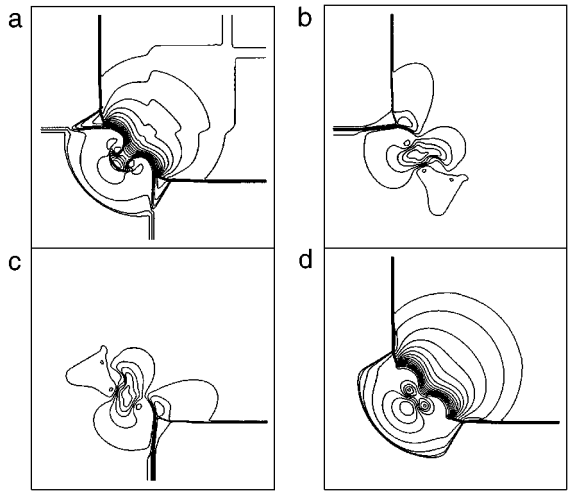


**FIG. 19.** High resolution results for a two-dimensional Riemann problem, a case with simple Mach reflection. The result is obtained using a $400 \times 400$ grid and the improved method with the update of the total kinetic energy. Contours of the solutions for (a) density, (b) particle velocity in the $x$-direction, (c) particle velocity in the $y$-direction, and (d) pressure are shown at time $t = 800$ $\mu$s.

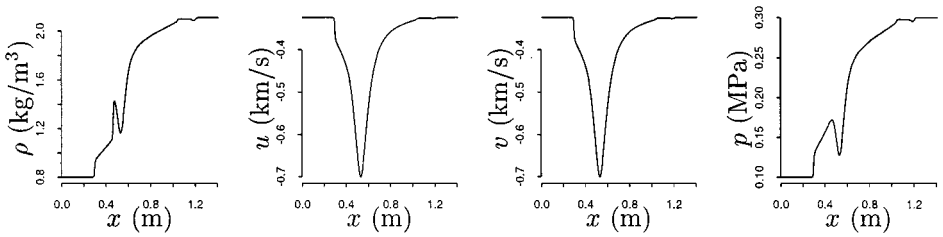


**FIG. 20.** Cross-sectional plots of $\rho$, $u$, $v$, and $p$ for the same run shown in Fig. 19 $x = y$.

plot, we observe sharp resolution of the primary shock waves and good behavior of the slip lines. The cross-sectional plots of $\rho$, $u$, $v$, and $p$ for the same run along the line $x = y$ provide an example of the basic structure of the solutions quantitatively. A detailed study of the algorithm to more general unstable interface problems such as the Kelvin–Helmholtz and Rayleigh–Taylor instabilities will be reported elsewhere in the future.

## 6. CONCLUSIONS

We have described an extension of a simple interface-capturing approach originally developed for compressible multicomponent flows with a stiffened gas equation of state to the more general case of a van der Waals-type fluid in more than one space dimension. The algorithm uses a mixture-type of the model equations written in a quasi-conservative form to ensure a consistent approximation of the energy equation near the interfaces where two or more fluid components are present in a grid cell. A standard high-resolution method based on the wave propagation formulation is employed to solve the proposed system, giving an efficient implementation of the algorithm. Numerical results present in the paper show that this is a viable approach in both one and two dimensions as applied in the method with the Roe solver to practical problems without introducing any spurious oscillations in the pressure near the interfaces.

To deal with a difficult slip line problem where there is a strong shear flow moving along the interface, we implement the two-dimensional method based on a shock-only Riemann solver with an additional update by the scheme to the total kinetic energy. Substituting the resulting kinetic energy to the formula for the pressure yields typically more accurate results than the uncorrected method near slip lines.

Ongoing work is to further improve upon efficiency and resolution of the algorithm by combining an adaptive mesh refinement and front tracking technqiues (cf. [4, 5, 40, 41]) to the existing computer program. Direct numerical simulation of practical problems such as the sonoluminescence model, the water-splashed problem, and shock waves in bubbly liquids will be considered in the future. Generalization of the algorithm to a more general equation of state such as the one appeared in [27, 28] will be looked at also.

## ACKNOWLEDGMENTS

This work was supported in part by National Science Council of Republic of China Grants NSC-86-2115-M-002-005 and NSC-87-2115-M-002-016. The author thanks Dr. Richard Saurel for his hard but pertinent criticisms that helped to improve the first draft of the manuscript.

## REFERENCES


1. R. Abgrall, How to prevent pressure oscillations in multicomponent flow calculations: A quasi conservative approach, *J. Comput. Phys.* **125**, 150 (1996).
2. M. Arora and P. L. Roe, On postshock oscillations due to shock capturing schemes in unsteady flows, *J. Comput. Phys.* **130**, 25 (1997).
3. D. S. Balsara, Riemann solver for relativistic hydrodynamics, *J. Comput. Phys.* **114**, 284 (1994).
4. M. J. Berger and P. Colella, Local adaptive mesh refinement for shock hydrodynamics, *J. Comput. Phys.* **82**, 64 (1989).
5. M. J. Berger and R. J. LeVeque, Adaptive mesh refinement using wave-propagation algorithms for hyperbolic systems, *SIAM J. Numer. Anal.* **35**, 2298 (1998).
6. E. L. Carstensen and L. L. Foldy, Propagation of sound through a liquid containing bubbles, *J. Acoust. Soc. Am.* **19**, 481 (1947).
7. Y. C. Chang, T. Y. Hou, B. Merriman, and S. Osher, A level set formulation of Eulerian interface capturing methods for incompressible fluid flows, *J. Comput. Phys.* **124**, 449 (1996).
8. J. D. Cheeke, Single-bubble sonoluminescence: Bubble, bubble, toil and trouble, *Can. J. Phys.* **75**, 77 (1997).
9. J. F. Clark, S. Karni, J. J. Quirk, P. L. Roe, L. G. Simmonds, and E. F. Toro, Numerical computation of two-dimensional unsteady detonation waves in high energy solids, *J. Comput. Phys.* **106**, 215 (1993).
10. P. Colella, Glimm's method for gas dynamics, *SIAM J. Sci. Stat. Comput.* **3**, 76 (1982).
11. P. Colella, Multidimensional upwind methods for hyperbolic conservation laws, *J. Comput. Phys.* **87**, 171 (1990).
12. P. Colella, R. E. Ferguson, and H. M. Glaz, Multifluid algorithms for Eulerian finite difference methods, preprint, 1994.
13. P. Colella and H. M. Glaz, Efficient solution algorithms for the Riemann problem for real gases, *J. Comput. Phys.* **59**, 264 (1985).
14. C. H. Cooke and T.-J. Chen, On shock capturing for pure wave with general equation of state, *Comm. Pure Appl. Numer. Meth.* **8**, 219 (1992).
15. R. Courant and K. O. Friedrichs, *Supersonic Flow and Shock Waves* (Wiley-Interscience, New York, 1948).
16. A. Crespo, Sound and shock waves in liquids containing bubbles, *Phys. Fluids* **12**, 2274 (1969).
17. W. S. Don and C. B. Quillen, Numerical simulation of shock-cylinder interactions: I. resolution, *J. Comput. Phys.* **122**, 244 (1995).
18. B. Einfeldt, C. D. Munz, P. L. Roe, and B. Sjogreen, On Godunov type methods near low densities, *J. Comput. Phys.* **92**, 273 (1991).
19. R. P. Fedkiw, T. Aslam, B. Merriman, and S. Osher, A non-oscillatory Eulerian approach to interfaces in multimaterial flows (the ghost fluid method), *J. Comput. Phys.* **152**, 457 (1999).
20. R. P. Fedkiw, X.-D. Liu, and S. Osher, *A General Technique for Eliminating Spurious Oscillations in Conservative Schemes for Multiphase and Multispecies Euler Equations*, CAM Report 97-27 (UCLA, 1997).
21. E. Fermi, *Thermodynamics* (Dover, New York, 1956).
22. P. Glaister, An approximate linearised Riemann solver for the Euler equations for real gases, *J. Comput. Phys.* **74**, 382 (1988).
23. E. Godlewski and P.-A. Raviart, *Numerical Approximation of Hyperbolic Systems of Conservation Laws*, Applied Mathematical Science, Vol. 118 (Springer-Verlag, Berlin/New York, 1996).
24. J. Grove, The interaction of shock waves with fluid interfaces, *Adv. Appl. Math.* **10**, 201 (1989).
25. J. Grove and R. Menikoff, The anomalous reflection of a shock wave at a material interface, *J. Fluid. Mech.* **219**, 313 (1990).
26. H. Hattori, The Riemann problem for a van der Waals fluid with entropy rate admissibility criterion–nonisothermal case, *J. Differential Equations* **65**, 158 (1986).
27. T. Hiroe, H. Matsuo, and K. Fujiwara, Numerical simulation of cylindrical converging shocks in solids, *J. Appl. Phys.* **72**, 2605 (1992).

28. R. Jeanloz, Shock wave equation of state and finite strain theory, *J. Geophys. Res.* **94**(B5), 5873 (1989).
29. S. Karni, Multicomponent flow calculations by a consistent primitive algorithm, *J. Comput. Phys.* **112**, 31 (1994).
30. S. Karni, Hybrid multifluid algorithms, *SIAM J. Sci. Comput.* **17**, 1019 (1996).
31. D. Kincaid and W. Cheney, *Numerical Analysis* (Brooks/Cole, 1990).
32. L. D. Landau and E. M. Lifshitz, *Fluid Mechanics* (Pergamon, New York, 1959).
33. R. Löfstedt, B. P. Barber, and S. J. Putterman, Toward a hydrodynamic theory of sonoluminescence, *Phys. Fluids A* **5**, 2911 (1993).
34. R. J. LeVeque, High resolution finite volume methods on arbitrary grids via wave propagation, *J. Comput. Phys.* **78**, 36 (1988).
35. R. J. LeVeque, Hyperbolic conservation laws and numerical methods, in Von Karman Institute for Fluid Dynamics, 1990. Lecture series on computational fluid dynamics 1990–1993.
36. R. J. LeVeque, *Numerical Methods for Conservation Laws*, second ed. (Birkhäuser, Basel, 1992).
37. R. J. LeVeque, Simplified multi-dimensional flux limiter methods, in *Numerical Methods for Fluid Dynamics*, edited by M. J. Baines and K. W. Morton (Oxford University Press, Oxford, 1993), p. 175.
38. R. J. LeVeque, High-resolution conservative algorithms for advection in incompressible flow, *SIAM J. Numer. Anal.* **33**, 627 (1996).
39. R. J. LeVeque, Wave propagation algorithms for multi-dimensional hyperbolic systems, *J. Comput. Phys.* **131**, 327 (1997).
40. R. J. LeVeque and K.-M. Shyue, One-dimensional front tracking based on high resolution wave propagation methods, *SIAM J. Sci. Comput.* **16**, 348 (1995).
41. R. J. LeVeque and K.-M. Shyue, Two-dimensional front tracking based on high resolution wave propagation methods, *J. Comput. Phys.* **123**, 354 (1996).
42. R. J. LeVeque and R. Walder, Grid alignment effects and rotated methods for computing complex flows in astrophysics, in *Notes on Numerical Fluid Mechanics*, edited by J. B. Vos, A. Rizzi, and I. L. Ryhming (Vieweg, Wiesbaden, 1992), Vol. 35.
43. R. L. LeVeque, CLAWPACK: A software package for solving multi-dimensional conservation laws, in *Proc. 5th Intl. Conf. Hyperbolic Problems* (World Scientific, Singapore, 1996), p. 188.
44. D. R. Lide, *Handbook of Chemistry and Physics*, 76th edition (CRC Press, Boca Raton, FL, 1996).
45. H. W. Liepmann and A. Roshko, *Elements of Gas Dynamics* (Wiley, New York, 1956).
46. X.-D. Liu, R. P. Fedkiw, and S. Osher, *A Quasi-Conservative Approach to the Multiphase Euler Equations without Spurious Pressure Oscillations*, CAM Report 98-11 (UCLA, 1998).
47. S. P. Marsh, *LASL Shock Hugoniot Data* (University of California Press, Berkeley, 1980).
48. R. G. McQueen, S. P. Marsh, J. W. Taylor, J. N. Fritz, and W. J. Carter, The equation of state of solids from shock wave studies, in *High Velocity Impact Phenomena*, edited by R. Kinslow (Academic Press, San Diego, 1970).
49. R. Menikoff and B. Plohr, The Riemann problem for fluid flow of real materials, *Rev. Mod. Phys.* **61**, 75 (1989).
50. G. H. Miller and E. G. Puckett, A high order Godunov method for multiple condensed phases, *J. Comput. Phys.* **128**, 134 (1996).
51. F. D. Murnaghan, *Finite Deformation of an Elastic Solid* (Wiley, New York, 1951).
52. H. Nagoya, T. Obara, and K. Takayama, Underwater shock wave propagation and focusing in inhomogeneous media, in *Proceedings of 19th Intl. Symp. on Shock Waves, Marseille* edited by R. Brun and L. Z. Dumitrescu (Springer-Verlag, Berlin, 1995), p. 439.
53. R. I. Nigmatulin, *Dynamics of Multiphase Media* (Hemisphere, New York, 1991).
54. E. S. Oran and J. P. Boris, *Numerical Simulation of Reactive Flow* (Elsevier, New York, 1987).
55. B. J. Plohr, Shockless acceleration of thin plates modeled by a tracked random choice method, *AIAA Journal* **26**, 470 (1988).
56. J. J. Quirk, A contribution to the great Riemann solver debate, *Intl. J. Numer. Meth. Fl.* **18**, 555 (1994).
57. J. J. Quirk and S. Karni, On the dynamics of a shock-bubble interaction, *J. Fluid Mech.* **318**, 129 (1996).

58. P. L. Roe, Fluctuations and signals—A framework for numerical evolution problems, in *Numerical Methods for Fluid Dynamics*, edited by K. W. Morton and M. J. Baines (Academic Press, San Diego, 1982), p. 219.
59. P. L. Roe, Upwind schemes using various formulations of the Euler equations, in *Numerical Methods for the Euler Equations of Fluid Dynamics*, edited by F. Angrand, A. Dervieux, J. A. Desideri, and R. Glowinski (SIAM, Philadelphia, 1985), p. 14.
60. R. Saurel and R. Abgrall, A simple method for compressible multifluid flows, *SIAM J. Sci. Comput.*, to appear, 1999.
61. R. Saurel and R. Abgrall, A multiphase Godunov method for compressible multifluid and multiphase flows, *J. Comput. Phys.* **150**, 425 (1999).
62. C. W. Schulz-Rinne, J. P. Collins, and H. M. Glaz, Numerical solution of the Riemann problem for two-dimensional gas dynamics, *SIAM J. Sci. Comput.* **14**, 1394 (1993).
63. K.-M. Shyue, An efficient shock-capturing algorithm for compressible multicomponent problems, *J. Comput. Phys.* **142**, 208 (1998).
64. K.-M. Shyue, A volume-of-fluid type algorithm for compressible two-phase flows, in *Proc. 7th Intl. Conf. Hyperbolic Problems*, edited by M. Fey and R. Jetsch (Birkhäuser, Basel, 1998), p. 895.
65. K.-M. Shyue, *An Eulerian Interface-Capturing Approach for Compressible Two-Phase Flow with van der Waals-Type Fluids*, Final report NSC87-2115-M-002-016 (National Science Council, Taiwan, R.O.C., 1998), unpublished. [Available on the web: `http://www.math.ntu.edu.tw/shyue/2phase.ps.gz`]
66. H. B. Stewart and B. Wendroff, Two-phase flows: Models and methods, *J. Comput. Phys.* **56**, 363 (1984).
67. G. Strang, On the construction and comparison of difference schemes, *SIAM J. Numer. Anal.* **5**, 506 (1968).
68. M. Sussman, A. S. Almgren, J. B. Bell, P. Colella, L. H. Howell, and M. L. Welcome, An adaptive level set approach for incompressible two-phase flows, *J. Comput. Phys.* **148**, 81 (1999).
69. M. Sussman, P. Smereka, and S. Osher, A level set method for computing solutions to incompressible two-phase flow, *J. Comput. Phys.* **114**, 146 (1994).
70. P. K. Sweby, High resolution schemes using flux limiters for hyperbolic conservation laws, *SIAM J. Numer Anal.* **21**, 995 (1984).
71. M. J. Tan and S. G. Bankoff, Strong shock waves propagating through a bubbly mixture, *Experiments in Fluids* **2**, 159 (1984).
72. H. S. Tang and D. Huang, A second-order accurate capturing scheme for 1D inviscid flows of gas and water with vacuum zones, *J. Comput. Phys.* **128**, 301 (1996).
73. E. F. Toro, A fast Riemann solver with constant covolume applied to the random choice method, *Intl. J. Numer. Meth. in Fluids* **9**, 1145 (1989).
74. H.-S. Tsien, One-dimensional flows of a gas characterized by van der Waals equation of state, *J. Math. Phys. Mass. Inst. Tech.* **25**, 301 (1947).
75. S. O. Unverdi and G. Tryggvason, A front-tracking method for viscous, incompressible, multifluid flows, *J. Comput. Phys.* **100**, 25 (1992).
76. L. van Wijngaarden, One-dimensional flow of liquids containing small gas bubbles, *Ann. Rev. Fluid Mech.* **4**, 369 (1972).
77. M. Watanabe and A. Prosperetti, Shock waves in dilute bubbly liquids, *J. Fluid Mech.* **274**, 349 (1994).
78. C. C. Wu and P. H. Roberts, A model of sonoluminescence, *Proc. R. Soc. London A* **445**, 323 (1994).
79. K. Xu, BGK-based scheme for multicomponent flow calculations, *J. Comput. Phys.* **134**, 122 (1997).
80. K. Xu and J. Hu, Projection dynamics in Godunov-type schemes, *J. Comput. Phys.* **142**, 412 (1998).
81. K. Yamada, H. Nagoya, and K. Takayama, Shock wave reflection and refraction over a two-fluid interface, in *Proceedings of 19th Intl. Symp. on Shock Waves, Marseille*, edited by R. Brun and L. Z. Dumitrescu (Springer-Verlag, Berlin, 1995), p. 299.
82. Y. B. Zel'dovich and Y. P. Raizer, *Physics of Shock Waves and High-Temperature Hydrodynamic Phenomena*, Vol. I & Vol. II (Academic Press, San Diego, 1967).